Laser-probing the rotational cooling of molecular ions by electron collisions

Ábel Kálosi,[1,2,*] Manfred Grieser,[1] Robert von Hahn,[1] Ulrich Hechtfischer,[1,†] Claude Krantz,[1,‡] Holger Kreckel,[1] Damian Müll,[1] Daniel Paul,[1] Daniel W. Savin,[2] Patrick Wilhelm,[1] Andreas Wolf,[1] and Oldřich Novotný[1]

[1] *Max-Planck-Institut für Kernphysik, Saupfercheckweg 1, D-69117 Heidelberg, Germany*
[2] *Columbia Astrophysics Laboratory, Columbia University, New York, NY 10027, USA*

(Dated: April 1, 2022)

We present state-selected measurements of rotational cooling and excitation rates of CH^+ molecular ions by inelastic electron collisions. The experiments are carried out at the Cryogenic Storage Ring, making use of a monoenergetic electron beam at matched velocity in combination with state-sensitive laser-dissociation of the CH^+ ions for simultaneous monitoring of the rotational level populations. Employing storage times of up to 600 s, we create conditions where electron-induced cooling to the $J = 0$ ground state dominates over radiative relaxation, allowing for the experimental determination of inelastic electron collision rates to benchmark state-of-the-art theoretical calculations. On a broader scale, our experiments pave the way to probe inelastic electron collisions for a variety of molecular ions relevant in various plasma environments.

Electron collisions with molecular ions are fundamental processes in partially ionized molecular gas, ranging from astrophysical environments and planetary atmospheres to low temperature plasma used in advanced technologies [1, 2]. Despite their fundamental relevance, detailed experimental data on the effect of electron collisions on the internal excitation of the molecular ions are essentially non-existent. Moreover, to enable computationally tractable calculations, most state-of-the-art theoretical methods require significant approximations [3], such as the Coulomb-Born (CB) [4–7] and R-matrix methods [8–15], which in this context have remained without experimental verification. For rotationally inelastic collisions between electrons and molecular ions, in particular, theoretical calculations have not yet converged [4–13, 16–18] and we are unaware of any previous state-resolved experimental cross section data that can guide the theory.

For illustration, we consider the case of molecular ions in cold astrophysical environments [19, 20]. They are mostly observed [21] by radio-astronomy via transitions between the lowest rotational states, requiring knowledge of the inelastic collision processes that contribute to rotational excitation and de-excitation. At the relevant temperatures of 10–100 K, the dominant partners for inelastic collisions are hydrogen atoms or molecules, and electrons [13, 18]. Electronic collisions are relevant even at the generally small electron density in the interstellar medium (typically $\sim 10^{-4}$ of hydrogen) because of their higher rate coefficients ($> 10^{-6}$ cm^3 s^{-1} at 10–100 K for dipolar molecular ions). For ions such as HCO^+, electron collisions are found to even dominate the inelastic rates [18].

To represent, in particular, the astrophysical conditions, relevant laboratory studies should ensure the low-density, binary-collision regime. Hence, very sensitive detection methods are required. Moreover, the internal molecular excitation must be probed for only a few populated rotational levels, corresponding to the cold astrophysical temperatures. We present such a measurement using methylidyne (CH^+) cations circulating in a cryogenic storage ring. There, the rotational level populations are subject to radiative cooling in the cryogenic environment and to controlled electron collisions in a merged, velocity-matched beam of electrons. We probe the evolution of the level populations as a function of storage time by resonant photodissociation. At effective temperatures of ~ 20 K for the radiation field and ~ 26 K for the electrons, we reach effective electron densities substantially above the critical density needed for collisional transition rates to dominate over the radiative ones. Hence, rotational cooling by inelastic electron collisions outperforms radiative cooling, leading to $J = 0$ as the dominant rotational level after a much shorter storage time than for radiative cooling alone. Using laser diagnostics, the electron-induced changes of the rotational populations are measured and compared to theory. This confirms recent predictions for the low-temperature inelastic rate coefficients of CH^+ and demonstrates that, in combination with suitable rotational diagnostics, cryogenic storage rings offer a platform to measure rotationally inelastic electron-collision rates for a wide range of molecular ions.

Merged-beams studies in room-temperature storage rings [22] demonstrated the effect of electron collisions on rotational excitation of HD^+ by measuring the fragmentation energies from dissociative recombination (DR) events. However, individual angular momenta J could not be resolved and the effect of electron collisions on the rotational populations was far from dominant. Cryogenic storage rings for molecular ions [23, 24] now enable state-selective studies for the lowest J-levels of elementary diatomic ions. These studies addressed spontaneous radiative relaxation of rotational excitation in a low-temperature blackbody field for CH^+ [25] and OH^- [26, 27]. Moreover, the rotational dependence of the low-energy DR rate was measured in electron collision experiments on HeH^+ [28]. The present work extends these studies by combining laser probing of the rotational level

populations of CH^+ ions with the collisional rotational cooling of these ions by a merged electron beam.

The experiments are performed in the cryogenic storage ring CSR [24] at the Max Planck Institute for Nuclear Physics in Heidelberg, Germany. A 280-keV beam of CH^+ ions with a broad J distribution is produced in a Penning ion source, electrostatically accelerated, and injected into the CSR, where the ions then circulate with a mean storage lifetime of $\sim$180 s. For rotational diagnostics, they are illuminated in a straight section of the ring with nanosecond laser pulses from an optical parametric oscillator (OPO) with a tunable wavelength near 300 nm. At certain wavelengths, CH^+ ions in specific low-J levels can be preferentially addressed by resonant photodissociation, as already demonstrated at CSR [25]. Neutral H atoms from the photodissociation leave the closed ion orbit at a downstream electrostatic deflector and are counted on a microchannel plate (MCP) detector [Fig. 1(a)].

On each revolution, the ions interact with the velocity-matched, collinear electron beam of the CSR electron cooler. The electron cooler delivers a continuous, nearly monoenergetic electron beam of $\sim$20 eV, guided by an axial magnetic field (10 mT in the interaction region) to yield a 10-mm diameter, nearly homogeneous current density profile in the collinear overlap region with the ion beam. The electron density is $7.0(6) \times 10^5$ cm^{-3} (here and below, the number in parentheses is the one-sigma uncertainty of the final digit) and the relative velocities are mainly transverse to the beam direction with an effective temperature $T_\perp \sim 26$ K [$k_B T_\perp = 2.25(25)$ meV with k_B being the Boltzmann constant; further discussed below]. The overlap region is housed in a biased drift tube where the electrons are decelerated to 11.8 eV, thus reaching the same velocity as the stored CH^+ ions over an effective matched-velocity overlap region of 0.79(1) m. The ion beam is centered within the electron beam and reaches an effective full width at half-maximum (FWHM) diameter of <6 mm after 10 s of phase-space cooling by the electrons [29]. The DR rate and its dependence on the electron–ion collision energy are measured using the MCP detector. The peak in the DR rate at the lowest achievable electron–ion collision energy serves for matching the average ion and electron beam velocities.

CH^+ [29] has an $X^1\Sigma^+$ ground state with a rotational constant of $\sim$13.9 cm^{-1} and a dissociation energy $D_0 = 32\,946.7(11)$ cm^{-1} [30]. A metastable $a^3\Pi$ state with $\sim$1.2 eV excitation energy and measured lifetime of $\sim$7 s [37] is strongly populated in the injected ion beam [29]. At a storage time $t \gtrsim 20$ s, radiative relaxation has progressed along the vibrational cascades (all having radiative lifetimes $\tau_r < 0.1$ s) while the rotational cascade then has essentially depopulated the $J \geq 4$ states [$\tau_r < 2$ s for $X^1\Sigma^+(v = 0)$]. The population in the metastable $a^3\Pi$ levels was monitored in situ by storage-time-dependent molecular-fragment imaging making use

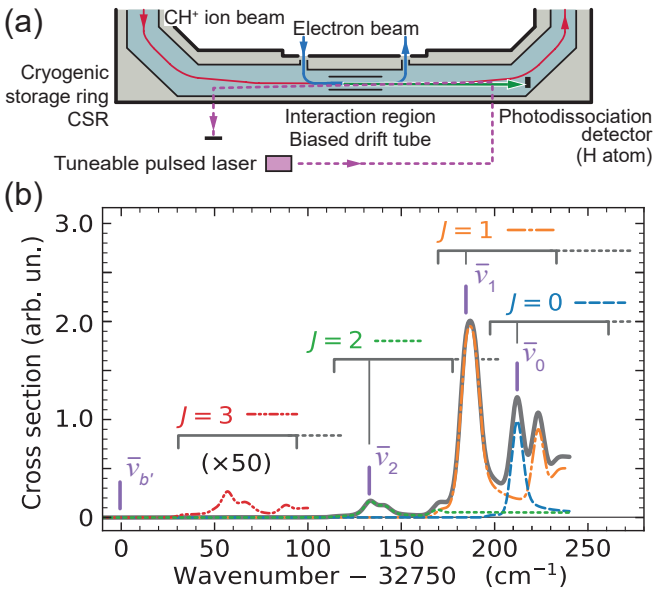

FIG. 1. (a) Schematic of the storage-ring section for laser probing and merged-beam electron–ion interaction. (b) Theoretical near-threshold photodissociation cross sections of CH^+ ions [25] in $J \leq 3$, weighted with a typical J distribution during rotational relaxation in the CSR and convolved with the laser lineshape (FWHM 6.1 cm^{-1}). Horizontal brackets: wavenumber ranges between the thresholds for $C^+(^2P_{1/2})$, lower, and $C^+(^2P_{3/2})$, upper, for the indicated J. Thick vertical lines mark the wavenumbers $\bar{\nu}_i$ ($i = 0 \ldots 2$) and $\bar{\nu}_{b'}$ where laser probing signals were accumulated. The probing wavenumbers are Doppler shift corrected, as explained in the supplemental material [29]. Individual J contributions (broken curves) add up to the total probed signal (full curve). The magnified contribution of $J = 3$ is shown up to the onset of its continuum level only.

of the unique signature of DR from these levels. Their fractional populations were found to be < 0.1 for $t > 25$ s and < 0.05 for $t > 40$ s [29]. For $t > 20$ s, we probe the populations of the remaining levels, $X^1\Sigma^+(v = 0, J \leq 3)$, via Feshbach resonances in near-threshold photodissociation [25, 30, 49]. In this process, optical transitions excite the $A^1\Pi$ electronic state which correlates to the atomic channel H + $C^+(^2P_{3/2})$ with a fine-structure excitation of 63.42 cm^{-1} [50] and supports vibrational energy levels above the H + $C^+(^2P_{1/2})$ channel. These levels dissociate by spin–orbit and rotational coupling while being long-lived enough to cause distinct resonances [30] in the near-threshold photodissociation spectrum.

Considering the initial $CH^+(X^1\Sigma^+, v = 0, J)$ levels, the photodissociation yield as a function of the photon energy has characteristic resonances for each J [Fig. 1(b)]. In our laser probing scheme, we use three photon wavenumbers $\bar{\nu}_i$ controlled by the OPO laser tuning, each situated near a J resonance peak for $J \leq 2$. Gated count rates R_i were accumulated in time windows synchronized with the arrival times of H atoms produced by

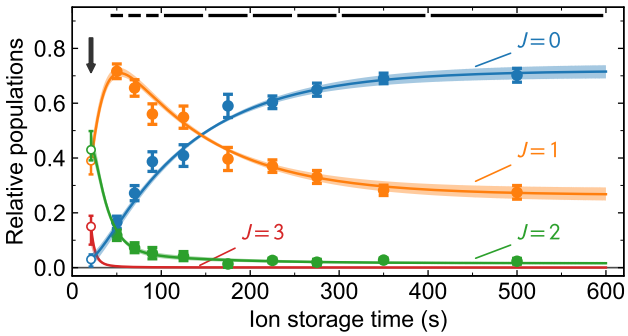

FIG. 2. Measured and modeled CH^+ rotational populations without electron interaction. Data p_J at $t > 40$ s (filled symbols and one-sigma uncertainties) were determined from the signals S_J at the J-specific laser-probing wavelengths ($J \leq 2$) averaged over the probing time windows indicated at the top (horizontal bars). Specialized laser scans (see the text) yielded populations $\tilde{p}_J$ (unfilled symbols) at $t = 21$ s (arrow) for $J \leq 3$. With these as initial conditions, the radiative model was fitted to the later p_0 and p_2 (p_1 follows as $1 - p_0 - p_2$) varying $T_{\rm low}$ and ϵ. Light colored bands: one-sigma uncertainties of the fitted model populations (including the $\tilde{p}_J$ uncertainties).

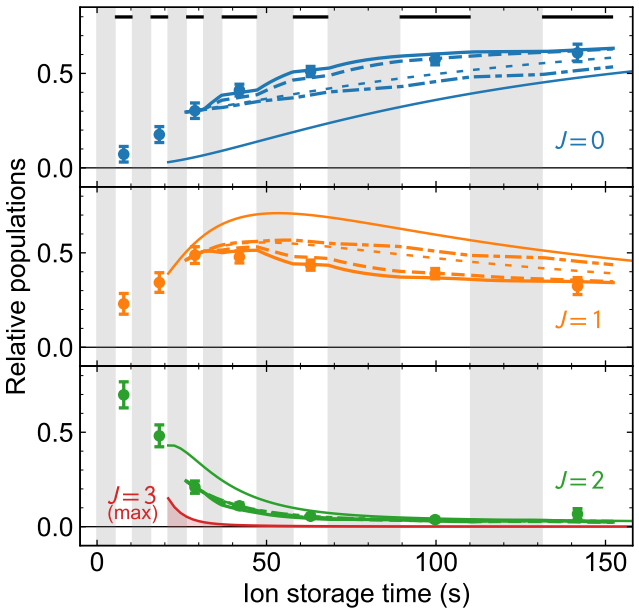

FIG. 3. Laser-probed CH^+ rotational populations p_J (symbols) with velocity-matched electrons applied in the shaded time windows. Thin full line: fitted $p_J(t)$ for radiative relaxation only from Fig. 2. The other lines show modeled evolutions starting from the $p_J(t = 28$ s) measured here. Short-dashed: radiation only; dash-dotted: depletion by J-dependent DR also included; long-dashed line: additionally including inelastic collisions using cross sections $\sigma^{\rm CB}_{J,J'}(E)$; thick full line: instead, using the R-matrix results [11] for the inelastic collisions cross sections. The red line and shaded area show the estimated maximum $J = 3$ population. Data points with one-sigma uncertainties.

the <10-ns laser pulses (repetition rate 20 s^{-1}), where the arrival times were evaluated as the time difference between the trigger signal of a laser pulse and the detection time of a corresponding counted particle. The background count rate R_b on the MCP from CH^+ collisions with residual gas molecules was recorded in the breaks between the synchronized gates. The wavenumbers were cycled and stayed ~ 4 s at each $\bar{\nu}$. The cycle included a further wavenumber $\bar{\nu}_{b'}$ below the $J = 3$ threshold to probe a rate $R_{b'}$ for all backgrounds, including any laser-induced one. The resonant laser-induced rates were normalized to the measured laser pulse energy ϵ_L and to R_b (proportional to the stored ion number), yielding the normalized signals $S_i = (R_i - R_{b'})/\epsilon_L R_b$. Based on updated molecular theory [25] and on a precise study of the resonance structure for our experimental parameters [29], these normalized signals can be expressed as $S_i = C \sum_J p_J \sigma_J(\bar{\nu}_i)$ with the known cross sections $\sigma_J(\bar{\nu}_i)$ and an overall normalization C. This relation is solved for the relative rotational populations p_J [29]. With electrons absent, we also performed finely spaced scans of $\bar{\nu}$ to align the experimental peaks with the J-dependent theoretical spectra. Moreover, the spectra from laser scans at $t = 14$–28 s were fitted with a linear combination of the calculated $\sigma_J(\bar{\nu})$ to derive populations $\tilde{p}_J$ ($J \leq 3$) [29] that we consider as the initial populations at $t = 21$ s for the rotational levels in the $X^1\Sigma^+, v = 0$ ground state.

As shown by the symbols in Fig. 2, relaxation by radiative transitions alone was probed for ten windows of t up to radiative equilibrium. The deduced $p_J(t)$ were fitted by the corresponding t-window averages of p_J from rate-equations which included spontaneous radiative decay as well as the transitions induced by a modeled blackbody radiation field of the CSR. In this radiative model [29], the spectral intensity is composed of a cryogenic component at a temperature $T_{\rm low}$ with a $1 - \epsilon$ fraction of the Planck blackbody spectrum plus a small fraction ϵ of a room-temperature (300 K) blackbody spectrum from radiation leaks into CSR. With the fitted parameters $T_{\rm low} = 14.6(21)$ K and $\epsilon = 1.03(28) \times 10^{-2}$, the radiative model well reproduces the measured $p_J(t)$ and is used to predict the J populations in the stored CH^+ ions when collisional cooling by the electrons is absent. Based on the in situ monitoring, the remaining small population in the metastable $a^3\Pi$ state is neglected. Assuming a purely thermal radiation field, its effective temperature $T_r^{\rm eff}$ can be derived directly from the asymptote of the population ratio between the $J = 0$ and 1 levels, $(p_1/p_0)_{\rm eq} = 0.39(5)$, which yields $T_r^{\rm eff} = 19.6(11)$ K.

The effect of low-energy electron collisions was then measured (Fig. 3) by merging the velocity-matched electron beam with the CH^+ ions. Phases with electrons on and off were alternated, with the electron-off phases serving as laser-probing time windows. This results in a duty

cycle for the inelastic electron interaction of ∼50%. The MCP detector was activated for the laser-probing only and turned off when the electrons were on, as the high DR event rate would saturate the MCP detector.

Compared to electrons off, the $J = 0$ level now becomes populated much faster. At only 30 s of storage, $p_0 \approx 0.3$ versus $p_0 < 0.1$ without electrons. Moreover, the asymptote of the $J = 1$ and 0 population ratio, representing the equilibrium between rotational cooling and excitation, rises significantly to $(p_1/p_0)_{\rm eq} = 0.53(13)$. Both observations reveal a strong collisional effect and directly show that in the low-temperature regime the critical electron density for the CH^+ $J = 0 \rightarrow 1$ transition is similar to or lower than our ring-averaged electron density $\bar{n}_e = 2.06(21) \times 10^4$ cm^{-3}. The larger collisional value of $(p_1/p_0)_{\rm eq}$ indicates a somewhat higher electron temperature as compared to $T_r^{\rm eff}$.

With the time dependence of the results in Fig. 3, we quantitatively test the electron-collision rate coefficients. We analyze the evolution of the p_J starting at $t = 28$ s, when the $J = 3$ relative population has dropped to $\lesssim 0.05$ and a three-level model ($J \leq 2$) is adequate. Even disregarding inelastic collisions, already DR as a potentially J dependent reactive process can influence the p_J. Therefore, in addition to the radiative rates, we must account for the variation of the p_J due to differences between the DR rate coefficients for the lowest J levels. These were obtained in a separate run within the same experiment, measuring the time dependence of the merged-beams J-averaged DR rate coefficient $\bar{\alpha}_{\rm DR}^{\rm mb}(t)$ in the velocity-matched beams over 100 s of storage. These measurements required the electron energy to be rapidly alternated from velocity-matching condition to higher values (0.2–4 eV collision energy). This led to modified $p_J(t)$ values that, during the times of detuned electron velocity, were again laser-monitored. Correlating the changes of these $p_J(t)$ with those of $\bar{\alpha}_{\rm DR}^{\rm mb}(t)$, differences between the J-specific DR rate coefficients could be derived [29]. The $p_J(t)$ modeled with radiative transitions plus J-selective depletion by DR, but still excluding inelastic collisions, are separately shown in Fig. 3.

To include the inelastic collisions, cross sections $\sigma_{J,J'}(E)$ as functions of the collision energy E are used [29] to determine merged-beams inelastic rate coefficients $\alpha_{J,J'}^{\rm mb}$, thus adding the related $J \rightarrow J'$ transitions to the rate equations for $p_J(t)$. We perform this step for $\sigma_{J,J'}(E)$ calculated in the CB approximation [4, 5, 7, 29] as well as from the most recent R-matrix calculations [11]. The latter are generally higher than the CB results by a factor of ∼1.6. The collision energy distribution used in the determination of $\alpha_{J,J'}^{\rm mb}$ is modeled for a set of electron temperatures $k_B T_\perp$ between 1.5 meV and 3.0 meV [29]. The modeled equilibrium population ratio $(p_1/p_0)_{\rm eq}$, largely governed by $\alpha_{1,0}^{\rm mb}/\alpha_{0,1}^{\rm mb}$, depends significantly on $k_B T_\perp$, but only weakly on the theoretical cross-section size. This size effectively cancels in the ratio $\alpha_{1,0}^{\rm mb}/\alpha_{0,1}^{\rm mb}$ as the cooling and excitation cross sections are related through detailed balance. Comparing [29] the model with the measured p_J at $t = 142$ s supports the experimental value of $k_B T_\perp = 2.25(25)$ meV [$T_\perp = 26(3)$ K].

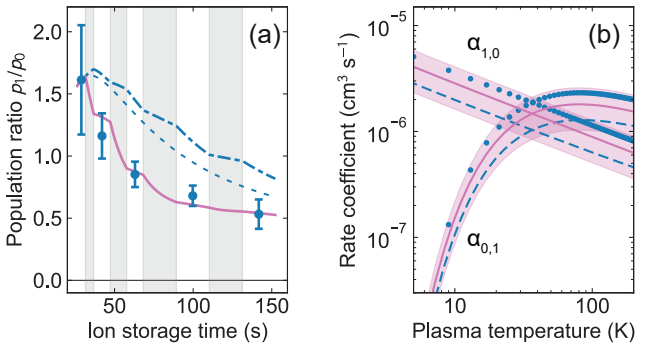

FIG. 4. (a) Population ratios p_1/p_0 corresponding to Fig. 3 (electrons applied in shaded time windows) with modeled evolutions starting from the measured populations at $t = 28$ s. Short-dashed: radiation only; dash-dotted: depletion by J-dependent DR also included; full line: additionally including inelastic collisions with the simplified $\hat{\sigma}_{J,J'}(E)$ and fitting for $\hat{\sigma}_{0,1}^0$. (b) Plasma rate coefficients $\alpha_{1,0}(T)$ and $\alpha_{0,1}(T)$ as constrained by the fitted $\hat{\sigma}_{0,1}^0$ (full lines and shaded one-sigma uncertainty), compared to R-matrix theory [11] (coalescing dots) and to the CB calculation (dashed line).

The data measured at intermediate times for $p_0(t)$ and $p_1(t)$ can then be compared to the model calculations employing the experimental $T_\perp$. This probes the absolute values of the inelastic rate coefficients, dominantly $\alpha_{1,0}^{\rm mb}$ and $\alpha_{0,1}^{\rm mb}$. As seen in Fig. 3 the data are remarkably well reproduced when using the R-matrix cross sections; slightly worse agreement is found for the CB approximation.

Comparison with theory is also possible considering the thermal rate coefficients implied by the experiment. For the relevant collision energies, the J-changing cross sections for an energy level pair spaced by $\Delta E_{J,J'}$ are well approximated by a simplified, single-parameter expression. For excitation ($J' > J$), the approximation is $\hat{\sigma}_{J,J'}(E) = \hat{\sigma}_{J,J'}^0 \Delta E_{J,J'}/E$ (where $E > \Delta E_{J,J'}$) with the threshold value $\hat{\sigma}_{J,J'}^0$ as only parameter. For deexcitation, detailed balance then yields, at all energies, $\hat{\sigma}_{J',J}(E) = \hat{g}\hat{\sigma}_{J,J'}^0 \Delta E_{J,J'}/E$ with $\hat{g} = (2J+1)/(2J'+1)$. An experimental value for $\hat{\sigma}_{0,1}^0$ can be obtained from the time dependence of the ratio p_1/p_0 starting at $t = 28$ s [Fig. 4(a)]. A fit of the parameter in the simplified model yields $\hat{\sigma}_{0,1}^0 = 1.07(23)_{\rm fit}(40)_{\rm syst} \times 10^4$ Å^2, where the first uncertainty stems from the fitting and the second one from the uncertainties in $T_\perp$, the initial condition at $t = 28$ s, and $\bar{n}_e$. (Simplified $\hat{\sigma}_{J,J+1}(E)$ and $\hat{\sigma}_{J+1,J}(E)$ for other level pairs were included in the model with their $\hat{\sigma}_{J,J+1}^0$ matching Ref. [11], but reducing them to

0 changed the fit result by only $< 0.02 \times 10^4$ Å^2.) The simplified cross sections with the experimental $\hat{\sigma}^0_{0,1}$ and the thermal electron energy distribution at a kinetic temperature T served to obtain the plasma rate coefficients $\alpha_{1,0}(T)$ and $\alpha_{0,1}(T)$, shown in Fig. 4(b). The corresponding R-matrix results [11] and the CB approximation lie well within the experimental one-sigma uncertainty range of ±43%.

This demonstrates the use of a merged-beams electron target in a cryogenic storage ring for quantitative probing of J-changing electron collisions between the lowest rotational levels in small molecular ions. The experimental method for rotational state probing used here, employing J-dependent resonances in single-step photodissociation, generally cannot be transferred to other ion species. However, effort is underway [51] to develop J-dependent photodissociation schemes for additional small ions in cryogenic storage rings. For most systems, such schemes will include intermediate laser excitation steps similar to the resonant multiphoton dissociation process earlier realized in ion traps [52]. It will then be possible to extend the measurements to other systems crucial for spectrocopic probing of the interstellar medium, such as HCO^+. The CSR merged-beams setup offers more options for controlling and probing the electron collisions, beyond what has been realized in the present survey. Thus, future experiments may focus on precisely probing the change of p_J in a given electron interaction period or apply detuned average velocities of the electron and ion beam. This will allow electron impact excitation and de-excitation cross sections of molecular cations to be investigated in more detail, over a wider range of electron collision energies relevant not only for astrophysical environments, and also for molecular plasma conditions in general.

Financial support by the Max Planck Society is acknowledged. A.K. and D.W.S. were supported in part by the U.S. National Science Foundation Division of Astronomical Sciences Astronomy and Astrophysics Grants program under AST-1907188. We thank C.J. Williams for the NIST close coupling code used in the resonant photodissociation calculations and A. Faure for supplying the R-matrix cross sections underlying the rate coefficients published in Ref. [11].

* email: abel.kalosi@mpi-hd.mpg.de
† Now at: ASML Nederland B.V., Veldhoven, The Netherlands
‡ Present address: GSI Helmholtz Centre for Heavy Ion Research, 64291 Darmstadt

[1] K. Bartschat and M. J. Kushner, Electron collisions with atoms, ions, molecules, and surfaces: Fundamental science empowering advances in technology, Proc. Natl. Acad. Sci. USA **113**, 7026 (2016).
[2] K. Bartschat, Electron collisions—experiment, theory, and applications, J. Phys. B: At. Mol. Opt. Phys. **51**, 132001 (2018).
[3] M.-L. Dubernet, M. H. Alexander, Y. A. Ba, N. Balakrishnan, C. Balança, C. Ceccarelli, J. Cernicharo, F. Daniel, F. Dayou, M. Doronin, F. Dumouchel, A. Faure, N. Feautrier, D. R. Flower, A. Grosjean, P. Halvick, J. Kłos, F. Lique, G. C. McBane, S. Marinakis, N. Moreau, R. Moszynski, D. A. Neufeld, E. Roueff, P. Schilke, A. Spielfiedel, P. C. Stancil, T. Stoecklin, J. Tennyson, B. Yang, A.-M. Vasserot, and L. Wiesenfeld, BASECOL2012: A collisional database repository and web service within the Virtual Atomic and Molecular Data Centre (VAMDC), Astron. Astrophys. **553**, A50 (2013).
[4] R. F. Boĭkova and V. D. Ob''edkov, Rotational and vibrational excitation of molecular ions by electrons, Zh. Eksp. Teor. Fiz. **54**, 1439 (1968) [Sov. Phys. JETP **27**, 772–774 (1968)].
[5] S.-I. Chu and A. Dalgarno, Rotational excitation of CH^+ by electron impact, Phys. Rev. A **10**, 788 (1974); Phys. Rev. A **12**, 725 (1975).
[6] S. S. Bhattacharyya, B. Bhattacharyya, and M. V. Narayan, Rotational excitation of molecular ions by electron impact under interstellar conditions, Astrophys. J. **247**, 936 (1981).
[7] D. A. Neufeld and A. Dalgarno, Electron-impact excitation of molecular ions, Phys. Rev. A **40**, 633 (1989).
[8] I. Rabadán, B. K. Sarpal, and J. Tennyson, Calculated rotational and vibrational excitation rates for electron–HeH^+ collisions, Mon. Not. R. Astron. Soc. **299**, 171 (1998).
[9] A. J. Lim, I. Rabadán, and J. Tennyson, Electron-impact rotational excitation of CH^+, Mon. Not. R. Astron. Soc. **306**, 473 (1999).
[10] A. Faure and J. Tennyson, Electron-impact rotational excitation of linear molecular ions, Mon. Not. R. Astron. Soc. **325**, 443 (2001).
[11] J. R. Hamilton, A. Faure, and J. Tennyson, Electron-impact excitation of diatomic hydride cations – I. HeH^+, CH^+, ArH^+, Mon. Not. R. Astron. Soc. **455**, 3281 (2016).
[12] K. Chakrabarti, A. Dora, R. Ghosh, B. S. Choudhury, and J. Tennyson, R-matrix study of electron impact excitation and dissociation of CH^+ ions, J. Phys. B: At. Mol. Opt. Phys. **50**, 175202 (2017).
[13] A. Faure, P. Halvick, T. Stoecklin, P. Honvault, M. D. Epée Epée, J. Z. Mezei, O. Motapon, I. F. Schneider, J. Tennyson, O. Roncero, N. Bulut, and A. Zanchet, State-to-state chemistry and rotational excitation of CH^+ in photon-dominated regions, Mon. Not. R. Astron. Soc. **469**, 612 (2017).
[14] J. R. Hamilton, A. Faure, and J. Tennyson, Electron-impact excitation of diatomic hydride cations II: OH^+ and SH^+, Mon. Not. R. Astron. Soc. **476**, 2931 (2018).
[15] B. Cooper, M. Tudorovskaya, S. Mohr, A. O'Hare, M. Hanicinec, A. Dzarasova, J. Gorfinkiel, J. Benda, Z. Mašín, A. Al-Refaie, P. Knowles, and J. Tennyson, Quantemol electron collisions (QEC): An enhanced expert system for performing electron molecule collision calculations using the R-matrix method, Atoms **7**, 97 (2019).
[16] A. S. Dickinson and D. R. Flower, Electron collisional excitation of interstellar molecular ions, Mon. Not. R. Astron. Soc. **196**, 297 (1981).

[17] D. R. Flower, Rotational excitation of HCO^+ by H_2, Mon. Not. R. Astron. Soc. **305**, 651 (1999).

[18] H. S. Liszt, Rotational excitation of simple polar molecules by H_2 and electrons in diffuse clouds, Astron. Astrophys. **538**, A27 (2012).

[19] J. H. Black, Molecules in harsh environments, Faraday Disc. **109**, 257 (1998).

[20] S. Petrie and D. K. Bohme, Ions in space, Mass Spectrometry Reviews **26**, 258 (2007).

[21] B. A. McGuire, 2018 census of interstellar, circumstellar, extragalactic, protoplanetary disk, and exoplanetary molecules, Astrophys. J. Suppl. Ser. **239**, 17 (2018).

[22] D. Shafir, S. Novotny, H. Buhr, S. Altevogt, A. Faure, M. Grieser, A. G. Harvey, O. Heber, J. Hoffmann, H. Kreckel, L. Lammich, I. Nevo, H. B. Pedersen, H. Rubinstein, I. F. Schneider, D. Schwalm, J. Tennyson, A. Wolf, and D. Zajfman, Rotational cooling of HD^+ molecular ions by superelastic collisions with electrons, Phys. Rev. Lett. **102**, 223202 (2009).

[23] H. T. Schmidt, Electrostatic storage rings for atomic and molecular physics, Phys. Scripta **T166**, 014063 (2015).

[24] R. von Hahn, A. Becker, F. Berg, K. Blaum, C. Breitenfeldt, H. Fadil, F. Fellenberger, M. Froese, S. George, J. Göck, M. Grieser, F. Grussie, E. A. Guerin, O. Heber, P. Herwig, J. Karthein, C. Krantz, H. Kreckel, M. Lange, F. Laux, S. Lohmann, S. Menk, C. Meyer, P. M. Mishra, O. Novotný, A. P. O'Connor, D. A. Orlov, M. L. Rappaport, R. Repnow, S. Saurabh, S. Schippers, C. D. Schröter, D. Schwalm, L. Schweikhard, T. Sieber, A. Shornikov, K. Spruck, S. Sunil Kumar, J. Ullrich, X. Urbain, S. Vogel, P. Wilhelm, A. Wolf, and D. Zajfman, The cryogenic storage ring CSR, Rev. Sci. Instrum. **87**, 063115 (2016).

[25] A. O'Connor, A. Becker, K. Blaum, C. Breitenfeldt, S. George, J. Göck, M. Grieser, F. Grussie, E. Guerin, R. von Hahn, U. Hechtfischer, P. Herwig, J. Karthein, C. Krantz, H. Kreckel, S. Lohmann, C. Meyer, P. Mishra, O. Novotný, R. Repnow, S. Saurabh, D. Schwalm, K. Spruck, S. Sunil Kumar, S. Vogel, and A. Wolf, Photodissociation of an internally cold beam of CH^+ ions in a cryogenic storage ring, Phys. Rev. Lett. **116**, 113002 (2016).

[26] C. Meyer, A. Becker, K. Blaum, C. Breitenfeldt, S. George, J. Göck, M. Grieser, F. Grussie, E. Guerin, R. von Hahn, P. Herwig, C. Krantz, H. Kreckel, J. Lion, S. Lohmann, P. Mishra, O. Novotný, A. O'Connor, R. Repnow, S. Saurabh, D. Schwalm, L. Schweikhard, K. Spruck, S. Sunil Kumar, S. Vogel, and A. Wolf, Radiative rotational lifetimes and state-resolved relative detachment cross sections from photodetachment thermometry of molecular anions in a cryogenic storage ring, Phys. Rev. Lett. **119**, 023202 (2017).

[27] H. Schmidt, G. Eklund, K. Chartkunchand, E. Anderson, M. Kamińska, N. de Ruette, R. Thomas, M. Kristiansson, M. Gatchell, P. Reinhed, S. Rosén, A. Simonsson, A. Källberg, P. Löfgren, S. Mannervik, H. Zettergren, and H. Cederquist, Rotationally cold OH^- ions in the cryogenic electrostatic ion-beam storage ring DESIREE, Phys. Rev. Lett. **119**, 073001 (2017); Phys. Rev. Lett. **121**, 079901 (2018).

[28] O. Novotný, P. Wilhelm, D. Paul, A. Kálosi, S. Saurabh, A. Becker, K. Blaum, S. George, J. Göck, M. Grieser, F. Grussie, R. von Hahn, C. Krantz, H. Kreckel, C. Meyer, P. M. Mishra, D. Muell, F. Nuesslein, D. A. Orlov, M. Rimmler, V. C. Schmidt, A. Shornikov, A. S. Terekhov, S. Vogel, D. Zajfman, and A. Wolf, Quantum-state-selective electron recombination studies suggest enhanced abundance of primordial HeH^+, Science **365**, 676 (2019).

[29] Supplemental material on the molecular parameters of CH^+, the experimental method, and the modelling of the inelastic rates, which contains Refs. [30–49].

[30] U. Hechtfischer, C. J. Williams, M. Lange, J. Linkemann, D. Schwalm, R. Wester, A. Wolf, and D. Zajfman, Photodissociation spectroscopy of stored CH^+ ions: Detection, assignment, and close-coupled modeling of near-threshold Feshbach resonances, J. Chem. Phys. **117**, 8754 (2002).

[31] P. F. Bernath, *Spectra of Atoms and Molecules*, 2nd ed. (Oxford University Press, New York, 2005).

[32] R. Hakalla, R. Kępa, W. Szajna, and M. Zachwieja, New analysis of the Douglas-Herzberg system ($A^1\Pi$-$X^1\Sigma^+$) in the CH^+ ion radical, Eur. Phys. J. D **38**, 481 (2006).

[33] U. Hechtfischer, J. Rostas, M. Lange, J. Linkemann, D. Schwalm, R. Wester, A. Wolf, and D. Zajfman, Photodissociation spectroscopy of stored CH^+ and CD^+ ions: Analysis of the $b^3\Sigma^-$–$a^3\Pi$ system, J. Chem. Phys. **127**, 204304 (2007).

[34] I. Kusunoki and C. Ottinger, Triplet $CH^+(CD^+)$ emission from chemiluminescent ion–molecule reaction $C^+(^4P)+ H_2(D_2)$, J. Chem. Phys. **73**, 2069 (1980).

[35] J. L. Doménech, P. Jusko, S. Schlemmer, and O. Asvany, The first laboratory detection of vibration-rotation transitions of $^{12}CH^+$ and $^{13}CH^+$ and improved measurement of their rotational transition frequencies, Astrophys. J. **857**, 61 (2018).

[36] M. Cheng, J. M. Brown, P. Rosmus, R. Linguerri, N. Komiha, and E. G. Myers, Dipole moments and orientation polarizabilities of diatomic molecular ions for precision atomic mass measurement, Phys. Rev. A **75**, 012502 (2007).

[37] Z. Amitay, D. Zajfman, P. Forck, U. Hechtfischer, B. Seidel, M. Grieser, D. Habs, R. Repnow, D. Schwalm, and A. Wolf, Dissociative recombination of CH^+: Cross section and final states, Phys. Rev. A **54**, 4032 (1996).

[38] Ğ. Barinovs and M. C. van Hemert, CH^+ potential energy curves and photodissociation cross-section, Chem. Phys. Lett. **399**, 406 (2004).

[39] D. A. Orlov, U. Weigel, M. Hoppe, D. Schwalm, A. S. Jaroshevich, A. S. Terekhov, and A. Wolf, Cold electrons from cryogenic GaAs photocathodes: Energetic and angular distributions, Hyperfine Interact. **146/147**, 215 (2003).

[40] S. Pastuszka, U. Schramm, M. Grieser, C. Broude, R. Grimm, D. Habs, J. Kenntner, H.-J. Miesner, T. Schüßler, D. Schwalm, and A. Wolf, Electron cooling and recombination experiments with an adiabatically expanded electron beam, Nucl. Instrum. Methods Phys. Res. Sect. A – Accel. Spectrom. Dect. Assoc. Equip. **369**, 11 (1996).

[41] G. I. Budker and A. N. Skrinskiĭ, Electron cooling and new possibilities in elementary particle physics, Usp. Fiz. Nauk **124**, 561–595 (1978) [Sov. Phys. Usp. **21**, 277–296 (1986)].

[42] C. Krantz, H. Buhr, M. Grieser, M. Lestinsky, O. Novotný, S. Novotny, D. Orlov, R. Repnow, A. Terekhov, P. Wilhelm, and A. Wolf, Transverse electron cooling of heavy molecular ions, Phys. Rev. Accel.

Beams **24**, 050101 (2021).

[43] P. A. M. van Hoof, R. J. R. Williams, K. Volk, M. Chatzikos, G. J. Ferland, M. Lykins, R. L. Porter, and Y. Wang, Accurate determination of the free–free Gaunt factor – I. Non-relativistic Gaunt factors, Mon. Not. R. Astron. Soc. **444**, 420 (2014).

[44] D. W. Hogg and D. Foreman-Mackey, Data analysis recipes: Using Markov Chain Monte Carlo, Astrophs. J. Suppl. Ser. **236**, 11 (2018).

[45] D. Foreman-Mackey, D. W. Hogg, D. Lang, and J. Goodman, emcee: The MCMC hammer, Publ. Astron. Soc. Pac. **125**, 306 (2013).

[46] Z. J. Mezei, M. D. Epée Epée, O. Motapon, and I. F. Schneider, Dissociative recombination of CH^+ molecular ion induced by very low energy electrons, Atoms **7**, 82 (2019).

[47] G. J. Vázquez, J. M. Amero, H. P. Liebermann, R. J. Buenker, and H. Lefebvre-Brion, Insight into the Rydberg states of CH, J. Chem. Phys. **126**, 164302 (2007).

[48] M. Larsson and A. E. Orel, *Dissociative Recombination of Molecular Ions* (Cambridge University Press, Cambridge, 2008).

[49] U. Hechtfischer, Z. Amitay, P. Forck, M. Lange, J. Linkemann, M. Schmitt, U. Schramm, D. Schwalm, R. Wester, D. Zajfman, and A. Wolf, Near-threshold photodissociation of cold CH^+ in a storage ring, Phys. Rev. Lett. **80**, 2809 (1998).

[50] A. Kramida, Yu. Ralchenko, J. Reader, and NIST ASD Team, NIST Atomic Spectra Database (ver. 5.8), [Online]. Available: `https://physics.nist.gov/asd` [2021, April 27]. National Institute of Standards and Technology, Gaithersburg, MD (2020).

[51] A. Znotins, F. Grussie, A. Wolf, X. Urbain, and H. Kreckel, An approach for multi-color action spectroscopy of highly excited states of H_3^+, J. Molec. Spectrosc. **378**, 111476 (2021).

[52] B. Roth, J. C. J. Koelemeij, H. Daerr, and S. Schiller, Rovibrational spectroscopy of trapped molecular hydrogen ions at millikelvin temperatures, Phys. Rev. A **74**, 040501 (2006).

Online Supplemental Material

Laser-probing the rotational cooling of molecular ions by electron collisions

Ábel Kálosi[1,2], Manfred Grieser[1], Robert von Hahn[1], Ulrich Hechtfischer[1,†], Claude Krantz[1,‡], Holger Kreckel[1], Damian Müll[1], Daniel Paul[1], Daniel W. Savin[2], Patrick Wilhelm[1], Andreas Wolf[1], Oldřich Novotný[1]

[1] *Max-Planck-Institut für Kernphysik, 69117 Heidelberg, Germany*

[2] *Columbia Astrophysics Laboratory, Columbia University, New York, NY 10027, USA*

[†] *Now at: ASML Nederland B.V., Veldhoven, The Netherlands*

[‡] *Present address: GSI Helmholtz Centre for Heavy Ion Research, 64291 Darmstadt*

In this Supplemental Material we present the background of our measurements on inelastic electron collisions with CH^+ and the modeling calculations we use for analyzing the results. We summarize the basic parameters of CH^+ and its radiative rotational cooling. Details are given for the experimental procedure of the laser measurements to determine rotational level populations. We then describe the parameters of our merged-beams electron–ion interaction setup and discuss how the measurements are affected by a metastable electronic state of CH^+ and by the rotational-level dependent dissociative recombination of this ion. We also summarize calculations on the inelastic electron collision cross sections and the resulting rotational transition rates for our study.

List of Supplemental Material

1. CH^+ energy levels and radiative cooling

The main properties of the molecular ground state and the first two bound, electronically excited levels of CH^+ are summarized in Table S1. This uses the experimental values [3] from the spectroscopy of the allowed $A\,^1\Pi$–$X\,^1\Sigma^+$ transitions. Moreover, the parameters deduced from experimental studies [4, 5] of the metastable $a\,^3\Pi$ level are included. For the rotational levels of the $X\,^1\Sigma^+$ ground state (rotational quantum number J), we use the recent rotational constants from terahertz spectroscopy [6] with relative deviations from Table S1 of $<10^{-4}$. This yields the energy levels given in Table S2.

For calculating the radiative transition probabilities between rotational levels J in the $X\,^1\Sigma^+$, $v = 0$ ground state we use the steps described earlier [7]. The Einstein coefficient for the spontaneous decay of level J is obtained as [2]

$$A_J \equiv A_{J\to J-1} = (16\pi^3/3\epsilon_0 h)\tilde{\nu}_{J-1}^3 \mu_0^2 J/(2J+1) \tag{S1}$$

where $\tilde{\nu}_J = (E_{J+1} - E_J)/hc$ with the level energies E_J and μ_0 is the permanent electric dipole moment of the $X\,^1\Sigma^+$, $v = 0$ CH^+ molecule. We use the most recent theoretical value [8] $\mu_0 = 0.6623\,ea_0 = 1.6834$ D ($1\ ea_0 = 2.541748$ D), calculated at an internuclear separation of $2.1530\ a_0 = 1.393$ Å. This separation agrees reasonably with the average internuclear distance r_0 for $X\,^1\Sigma^+$, $v = 0$ of Table S1. In these equations, c is the velocity of light, ϵ_0 the vacuum permeability, h Planck's constant and e the elementary charge.

TABLE S1. Experimental values for the molecular parameters in the vibrational ground states of the three lowest electronic levels of CH^+. The $X\,^1\Sigma^+$, $v = 0$ dissociation energy to $C^+(^2P_{1/2}) + H$ is 32 946.7(11) cm^{-1} [1]. B_0 and D_0 here are the spectroscopic constants in the usual rotational term definition, see Eq. (6.47) in Ref. [2]; indices 0 refer to vibrational quantum number $v = 0$ and e to the minimum of the electronic potential; ω_e is the vibrational constant; r_e, r_0 are internuclear distances; column T_e lists the electronic term value unless noted otherwise. (D_0 denotes the dissociation energy in the main paper.)

Level	T_e (cm^{-1})	B_0 (cm^{-1})	D_0 ($10^{-3}\,cm^{-1}$)	ω_e (cm^{-1})	B_e (cm^{-1})	r_e (Å)	r_0[a] (Å)
$X\,^1\Sigma^+$, $v = 0$[b]	0	13.93070(19)	1.3761(21)	2857.561(22)	14.177461(75)	1.1308843(30)	1.1409
$a\,^3\Pi$, $v = 0$[c]	9530(50)[d]	13.7770(34)	1.4760(70)	2631(30)[e]	14.08(2)	1.1348(8)	1.147
$A\,^1\Pi$, $v = 0$[b]	24118.726(14)	11.42351(18)	1.9800(19)	1864.402(22)	11.88677(72)	1.235053(37)	1.2598

[a] Scaled by using $r_0 = (B_e/B_0)^{1/2} r_e$; rounded value
[b] Data from Ref. [3]
[c] Data from Ref. [4] unless stated otherwise in this row.
[d] Band origin of the $a\,^3\Pi$-$X\,^1\Sigma^+$, v = (0-0) band ([4], Table IX)
[e] Ref. [5] with uncertainty estimated from remark included there

The property of the ambient radiation field relevant for absorption and total emission on a rotational transition with wavenumber $\tilde{\nu}_J$ is the occupation number $n(\tilde{\nu}_J)$ of the vacuum modes at $\tilde{\nu}_J$, which for a thermal radiation field at a temperature T_r is

$$n(\tilde{\nu}_J) \equiv n_{\rm th}(\tilde{\nu}_J, T_r) = [\exp(hc\tilde{\nu}_J/k_B T_r) - 1]^{-1} \tag{S2}$$

with the Boltzmann constant k_B. The decay rate by spontaneous and stimulated transitions from a level J into the next lower one is then given as

$$k^{\rm em}_{J\to J-1} = A_J[1 + n(\tilde{\nu}_{J-1})] \tag{S3}$$

while the excitation rate by radiative absorption from J into the next higher level is

$$k^{\rm abs}_{J\to J+1} = A_{J+1} n(\tilde{\nu}_J)(2J+3)/(2J+1). \tag{S4}$$

We use a superposition of two thermal components, one at $T_r = 300$ K at a small relative fraction ϵ and a main component at an effective cold radiation temperature $T_{\rm low}$, ($T_r = T_{\rm low}$), where $T_{\rm low}$ is fitted to the radiative cooling data. This yields the effective occupation number

$$n(\tilde{\nu}_J) = \epsilon n_{\rm th}(\tilde{\nu}_J, 300\ {\rm K}) + (1-\epsilon) n_{\rm th}(\tilde{\nu}_J, T_{\rm low}). \tag{S5}$$

When the CH^+ ions begin to be stored in the CSR after their production in the ion source, a significant fraction of them is found to populate the metastable $a\,^3\Pi$ state. Most levels (except the $a\,^3\Pi, v = 0, J = 0,\ f$ symmetry level, which is expected to be much longer lived [4] and is further discussed in Supplemental Sec. 7) decay with an average lifetime τ_m that was previously measured [9] to be close to 7 s. As long storage times up to 600 s are the main concern of this work, we begin modeling the J level populations in the $X\,^1\Sigma^+,\ v = 0$ ground state at a time of 21 s ($> 2\ \tau_m$),

TABLE S2. Rotational energy levels and Einstein coefficients for spontaneous decay of CH^+ for $X\,^1\Sigma^+$, $v = 0$.

J	Energy		A_J	$1/A_J$
	(cm^{-1})	(eV)	(s^{-1})	(s)
0	0	0	0	
1	27.86	0.003454	0.00640	156.1
2	83.54	0.010357	0.0614	16.29
3	167.0	0.02070	0.2213	4.52
4	278.1	0.03448	0.524	1.846
5	416.7	0.05166	1.076	0.929

starting with the measured populations of the lowest rotational levels $J = 0 \ldots 3$ in $X\,^1\Sigma^+$, $v = 0$. After this time, we neglect all population in higher excited levels of the $a\,^3\Pi$ metastable state that could decay into the selected low-J levels based on the experimentally observed disappearance of the fraction of the dissociative recombination (DR) signal which we can uniquely attribute to the metastable $a\,^3\Pi$ state by storage-time dependent molecular fragment imaging (further discussed in Supplemental Sec. 7).

2. CH^+ storage and laser probing of rotational energy levels

The method for laser probing of rotational levels is similar to that used in previous work [10] at the CSR. Pulses from a tunable optical parametric oscillator (OPO) laser (Ekspla NT342b, repetition rate 20 Hz) are directed into the CSR. Conditions different in the present experiment are discussed in the following. In the present setup, the laser counterpropagates relative to the ion beam (see Fig. S1) with a grazing angle of ∼1.5°. The laser wavelength (near 306 nm) is continuously monitored by a wavemeter (HighFinesse/Ångstrom Laser Spectrum Analyzer LSA UV-I, HighFinesse GmbH, Tübingen, Germany). Hence, the applied laser wavenumber $\tilde{\nu}_L$ is specified with ∼0.1 cm^{-1} stability over the duration of the experiment and a calibration uncertainty of $\lesssim$1 cm^{-1}. In addition to $\tilde{\nu}_L$ the wavemeter yields the spectral width of the applied laser light. For modeling the photodissociation spectrum, we use a Gaussian distribution of $\tilde{\nu}_L$ with a full width at half maximum (FWHM) of 6.1(3) cm^{-1} [$\sigma_{\tilde{\nu}_L} = 2.6(1)$ cm^{-1}]. The laser pulse energy is measured pulse by pulse (see power monitors in Fig. S1) and variations of the pulse energy ϵ_L transmitted through the CSR (typically 0.1–0.2 mJ) are measured with $\lesssim$5% uncertainty for normalizing the photodissociation signal to the irradiated photon flux.

The CH^+ ions are stored at a beam energy near 279.5 keV with run-by-run variations monitored

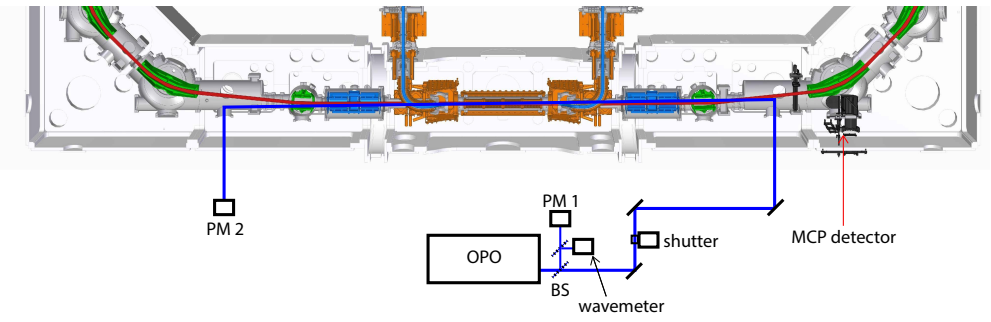

FIG. S1. View of the experimental section of the CSR with the electron beam setup in the center, the MCP detector, and the laser beam path. Red line: ion beam; bright blue curve: electron beam; darker blue line: laser beam. PM1, PM2: power monitors. BS: beam splitter.

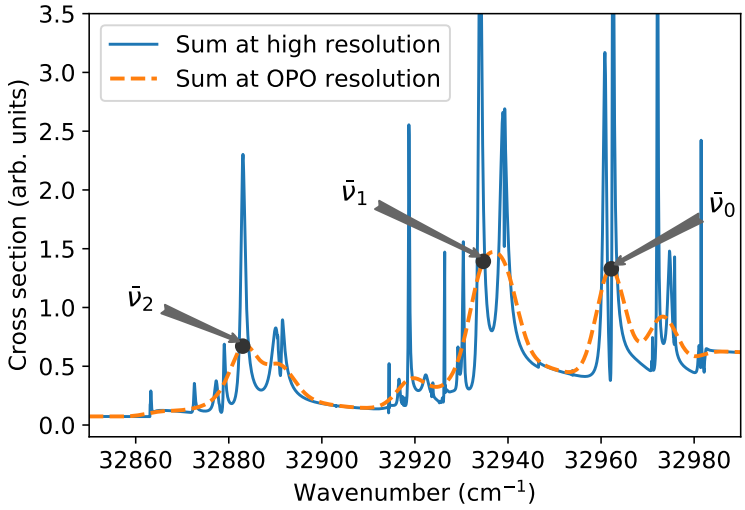

FIG. S2. Calculated near-threshold photodissociation spectrum of CH^+ for a rotational temperature of 77 K (mainly $J = 0 \ldots 2$) including natural resonance broadening only (blue line) and at the present resolution of 6.1 cm^{-1} (FWHM) (yellow dashed line). The probing wave numbers $\tilde{\nu}_{0\ldots2}$ are marked.

on an $\sim 10^{-4}$ (0.03 keV) level by ion revolution frequency measurements. The absolute energy has a relative uncertainty of $\sim 3 \times 10^{-3}$, corresponding to 0.8 keV. The beam velocity is βc (with c the velocity of light) where $\beta \approx 0.00679$, with its relative variations being monitored with $\sim 0.5 \times 10^{-4}$ uncertainty for the purpose of Doppler correction of the laser wave number. The typical number N_i of ions stored in the CSR is 10^7. The overlap length of the ion beam with the grazing laser beam is $l_L \approx 0.4$ m, corresponding to $\sim$1% of the CSR circumference. This yields an ion number on the order of 10^5 in the laser overlap region. For recombination rate measurements N_i was reduced by a factor of $\sim 10^1$ to avoid saturating the neutral product detector.

By the Doppler correction, the wave number in the ion rest frame ($\tilde{\nu}$) is obtained from the laser wave number $\tilde{\nu}_L$ as

$$\tilde{\nu} = \tilde{\nu}_L \sqrt{1-\beta^2}/(1-\beta\cos\theta) \tag{S6}$$

The Doppler correction $\tilde{\nu} - \tilde{\nu}_L \approx 224$ cm^{-1} can be monitored for each run with an uncertainty of $\sim 0.5 \times 10^{-4}$ (0.01 cm^{-1}), while the uncertainty of the absolute size of the Doppler correction is $\sim 1.5 \times 10^{-3}$ (0.35 cm^{-1}). Owing to the low beam velocity of the present experiment, this uncertainty is about a factor of 3 lower than in the CH^+ photodissociation experiment at the TSR ($\beta \approx 0.034$) [1], where the Doppler correction constitutes the dominant component of the uncertainty (1.1 cm^{-1}) in the CH^+ dissociation energy measured by that experiment.

The microchannel plate (MCP) detector (see Fig. S1) detects neutral fragments from the interaction section of the CSR. The fragments induced by laser pulses reach the detector with a time spread

of $l_L/\beta c \approx 0.2$ μs, spaced by 50 ms corresponding to the pulse repetition frequency. In the breaks between pulses, a continuous neutralization rate of the circulating CH^+ ions of the order of 10^3 s^{-1} is observed, stemming from the CH^+ collisions with the residual gas. Laser-induced neutral count rates R_i were recorded in time gates of 0.6 μs duration synchronized with the laser pulses at wavenumbers $\tilde{\nu}_i$ ($i = 0 \ldots 2$) and $\tilde{\nu}_{b'}$ [see Fig. 1(b) of the main paper]. The value $\tilde{\nu}_{b'} = 32\,750$ cm^{-1} was added to the probing wavenumbers in order to monitor the full background rate $R_{b'}$, which includes any laser-induced events not related to the $J \leq 3$ levels of $X\,^1\Sigma^+$, $v = 0$ CH^+. Moreover, a summed rate R_b for the continuous background from any neutrals formed in collisions of CH^+ ions with residual gas molecules was obtained from a 90-μs gate ending 12 μs before and another 40-μs gate starting 2.4 μs after each laser pulse. Together with the laser pulse energy ϵ_L, the normalized photodissociation signal is found as

$$S_i = S(\tilde{\nu}_i) = (R_i - R_{b'})/\epsilon_L R_b. \tag{S7}$$

To yield the photodissociation signals, pulses at a given laser wavenumber were typically repeated during ~ 4 s before setting the next value of $\tilde{\nu}_i$ ($i = 0 \ldots 2$) or $\tilde{\nu}_{b'}$ in the measurement cycle. Doppler corrected values are given for all probing wave numbers.

The rotational probing makes use of the resonant structure of the near-threshold CH^+ photodissociation, in which rotationally resolved predissociation resonances are observed and are found to be in excellent agreement with theoretical predictions. The underlying theory uses experimentally adjusted fine-structure resolved molecular potential curves and is based on Hechtfischer *et al.* [1] and Barinovs and van Hemert [11], with details discussed in the supplement of O'Connor *et al.* [10]. Using the calculated cross sections $\sigma_J(\tilde{\nu})$ for separate initial $CH^+(J)$ ions, a rotationally averaged spectrum

$$\bar{\sigma}(\tilde{\nu}) = \sum_{J=0}^{J_{\max}} p_J \sigma_J(\tilde{\nu}) \tag{S8}$$

($J_{\max} = 5$) is shown in Fig. S2 after convolution over a Gaussian broadened wavenumber distribution, illustrating the present experimental resolution. The rotational populations p_J are set for a thermal distribution with a rotational temperature at the upper end of the range of interest here, yielding dominant resonant contributions for $J = 0...2$, together with small, smooth contributions for (mainly) $J = 3$. In contrast to previous work [10] at CSR, the data are not acquired at full two-dimensional (time and wavenumber) resolution, but at the set $\tilde{\nu}_i$ of probing wave numbers only.

For rotational probing, the measured signals $S_i = S(\tilde{\nu}_i)$, with S from Eq. (S7), are expressed as

$$S_i = C \sum_{J=0}^{J_{\max}} Q_{Ji}\, p_J \tag{S9}$$

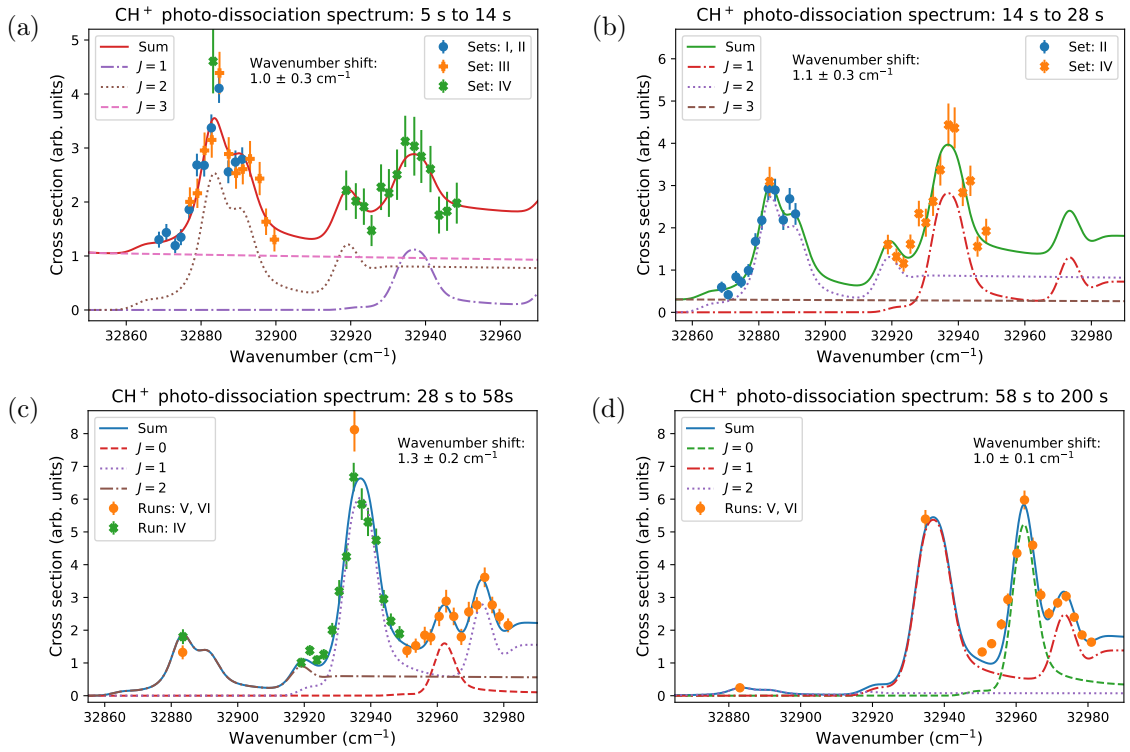

FIG. S3. Preparative laser scans of the CH^+ photodissociation signal for the storage time ranges given in the headings, showing sequence labels of the experimental runs and the individually fitted values of the wave number shift $\delta\tilde{\nu}$ discussed in the text. Individual J components of the fitted convoluted spectra are distinguished by line styles according to the legends.

with $J_{\max} = 2$ and the probing amplitudes $Q_{Ji} = \sigma_J(\tilde{\nu}_i - \delta\tilde{\nu})$. Detailed scans of the photodissociation signal (Fig. S3) were performed for calibrating the probing amplitudes and in particular the shift $\delta\tilde{\nu}$, which accounts for the residual uncertainty of the absolute wave number scale and the dissociation energy D_e of CH^+. In fact, these scans already observe the temporal change of the rotational populations p_J. Considering the radiative lifetimes of the J levels in the $X^1\Sigma^+, v = 0$ ground state (Table S2), significant contributions are expected to include $J = 0 \ldots 3$ for $t \gtrsim 5$ s and $J = 0 \ldots 2$ for $t \gtrsim 20$ s. The spectra observed in the indicated time windows were fitted to theoretical cross sections

$$S(\tilde{\nu}) = \sum_{J=0}^{J_{\max}} c_J \sigma_J(\tilde{\nu} - \delta\tilde{\nu}) \tag{S10}$$

with $J_{\max} = 3$ in Fig. S3(a), (b) and $J_{\max} = 2$ in Fig. S3(c), (d).

The ensemble of fit results shows that, relating to the $\tilde{\nu}$ scale of the applied wavemeter after the Doppler correction, the probing amplitudes can be obtained from the calculated, Gaussian convoluted cross sections when shifting the wavenumber scale of these results up by $\delta\tilde{\nu} = 1.0(1)$ cm^{-1}. The fitted relative amplitudes of the J-specific contributions in the time windows of Fig. S3(b) and (c) then allow us to derive the rotational populations within the $X^1\Sigma^+$ electronic state.

TABLE S3. Experimentally derived relative populations $\tilde{p}_J$ at $t = 21$ s, the start of the radiative relaxation model in the $X\,^1\Sigma^+$, $v = 0$ level. The uncertainties resulting from the fitting procedure are given for the last digit as upper and lower indices at a confidence level corresponding to a one-sigma uncertainty in the symmetric case.

J	$\tilde{p}_J$
0	0.03^{-3}_{+2}
1	0.39^{-5}_{+5}
2	0.43^{-4}_{+7}
3	0.15^{-7}_{+4}

The purpose of the measurements is to track the rotational populations in the $X^1\Sigma^+$ electronic state once that its feeding from the metastable $a\,^3\Pi$ state, with a measured average lifetime 7(1) s, can be neglected. We consider that we can neglect this feeding for storage times $t > 21$ s. From the results of Fig. S3(b) and (c) (with only a minor effect of the $a\,^3\Pi$ in the earlier one of these time windows), we estimate the starting populations in the $J = 0 \ldots 3$ levels of the $X^1\Sigma^+, v = 0$ ground state as given in Table S3. Effects of $a\,^3\Pi$ decay in the earlier one of these time windows is included in the given uncertainties. Populations in $J \geq 4$ rotational levels with lifetimes of <2 s are neglected.

3. Merged-beams electron collisions

The electron beam is merged with the circulating ion beam (see Fig. S1) with the help of a bent magnetic guiding field (20 mT in the bending regions and 10 mT in the overlap region with the ion beam). After being transported from the electron source at 20 eV, the electrons are decelerated in 0.85 m long drift tube to an energy of 11.79 eV, at which the beam velocity is matched to that of the stored ion beam (279.4 keV kinetic energy). The velocity distribution in the co-moving frame of the electron beam is anisotropic with respect to the beam direction with a transverse temperature $T_\perp$ and a longitudinal temperature $T_\parallel$. The electrons are emitted from a laser-illuminated photocathode operated near room temperature. It was shown [12] that the transverse temperatures of the emitted electrons then approach the bulk temperature (i.e., thermal energy $\gtrsim 26$ meV/k_B). The magnetic guiding field strength at the cathode exceeds the field strength in the interaction region by a factor of 20. Correspondingly, through the inverse magnetic-bottle effect, the transverse temperature $T_\perp$ in the interaction region is reduced compared to the emission temperature by approximately this factor [13] (i.e., $T_\perp \gtrsim 1.3$ meV). From initial operating experience at the CSR electron cooler, $k_B T_\perp$ is estimated to be somewhat larger than the theoretical limit (1.3 meV) and to lie between 1.5 meV

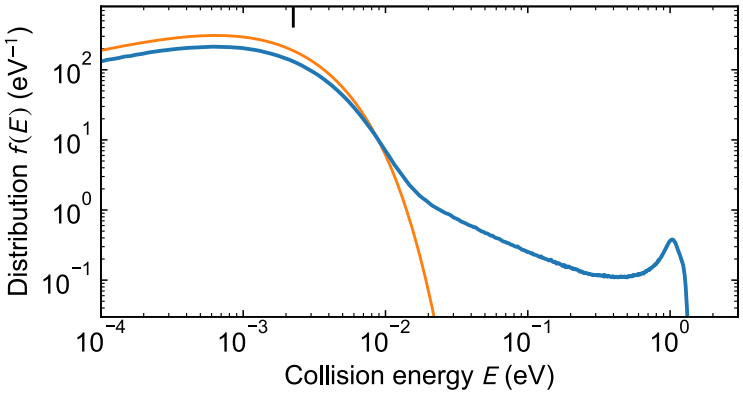

FIG. S4. Collision energy distributions (normalized) in the merged electron and ion beams at matched averaged beam velocities. Blue: Distribution from a Monte-Carlo simulation with $k_B T_\perp = 2.25$ meV (vertical mark at the top), including the experimental beam and drift-tube geometry, and the acceleration voltage fluctuations. Orange: Flattened Maxwellian energy distribution $f(E)$ from Eq. (S11) of the same $T_\perp$, determined such that $af(E)$ with $k_B T_\parallel = 0.59$ meV and $a = 0.693$ fits the simulated data at $E < k_B T_\perp$.

and 3 meV. In Supplemental Sec. 6 we discuss how we determined the best-fit value of $k_B T_\perp$ for this work.

The current profile of the electron beam was measured and is approximated by a cylindrical beam with a diameter of $2\rho = 10.2(5)$ mm in the interaction region.

While the relative velocity between electrons and ions is minimized by adjusting the precise electron velocity such that the electron cooling effect [14] on the ion beam is maximized, the velocity spread due to the beam temperatures leads to finite collision energies. Moreover, in the merging regions, electrons and ions interact at increased relative velocities. Using the geometry of the merging regions and the deceleration fields around the drift tube, the relative velocities are modeled by Monte-Carlo integration over the complete ion beam length of $l_0 = 1.136(14)$ m where both, electrons and ions, are present. This model also takes into account the electron beam temperatures (assuming Maxwellian velocity distributions) and the experimental ripple and noise on the voltage difference between the cathode and the interaction drift tube. Based on measurements for the situation during the CH^+ beam time, root mean square (r.m.s.) voltage fluctuations of 0.1 V are inserted in the model calculations. The resulting collision energy distribution $f(E)$ is shown in Fig. S4 for $k_B T_\perp = 2.25$ meV. The low-energy part ($E < k_B T_\perp$) can be very well fitted by the scaled energy distribution, $af(E)$, resulting from a bi-modal Maxwellian electron velocity distribution, with the normalized energy distribution reading

$$f(E) = \frac{1}{\zeta k_B T_\perp} e^{-E/k_B T_\perp} \operatorname{erf}\left(\zeta \sqrt{\frac{E}{k_B T_\parallel}}\right) , \quad \zeta = \sqrt{1 - \frac{T_\parallel}{T_\perp}} . \tag{S11}$$

The parameters of this fit are a and $T_\parallel$. The case shown in Fig. S4 leads to a fitted $k_B T_\parallel = 0.59$ meV, with this value being dominated by the effect of the electron beam acceleration voltage fluctuations. Moreover, the fraction of the modeled distribution fitted by the normalized function of Eq. (S11) is $a = 0.693$. Hence, ∼70% of the total ion–electron overlap length, corresponding to $\hat{l}_0 = a l_0 = 0.79(1)$ m, contributes with a narrow energy distribution ($E \lesssim 2k_B T_\perp$), while for ∼30% of l_0 the effective collision energy distribution is much wider with up to ∼1 eV of collision energy.

For the laser probing studies of rotationally inelastic collisions, reported here, the electron current was 18.5 μA. Together with the measured effective electron beam radius and the electron velocity in the central part of the interaction region, this yields an electron density of $n_e = 7.0(6) \times 10^5$ cm^{-3}, where the uncertainty is dominated by the knowledge of the electron current profile.

Dissociative recombination (DR) measurements used the same MCP detector (see Fig. S1) as that applied for the photodissociation measurements. In DR measurements, this detector continuously counts the neutral products from the electron–ion interaction region and also analyzes their kinetic energy release (KER) by measuring the transverse distance between the pairs of neutrals formed by DR.

For any electron-induced process (such as DR or inelastic collisions) the energy dependent cross section $\sigma(E)$ leads to a merged-beams rate coefficient

$$\alpha^{\mathrm{mb}} = \sqrt{\frac{2}{m}} \int_0^\infty f(E) \sqrt{E} \sigma(E) dE \tag{S12}$$

where m is the electron mass.

Based on the experience that by optimizing the electron cooling the ion beam is approximately centered within the electron beam, we assume concentric beams for our modeling of the experimental situation. The ion beam profile in the interaction region is measured by imaging the center-of-mass of coincident two-fragment DR events on the imaging detector and derived from these data by taking into account the projection of the neutral fragment trajectories from the interaction region to the detector. Here, the ion beam size and its divergence are assumed to be related [15] by the known focusing properties of the storage ring [16]. The determined r.m.s. ion beam sizes σ_x in the horizontal direction (bending plane of the storage ring) and the vertical size σ_y, reached after after electron cooling times of $t = 10$ s and 20 s, are listed in Table S4. Assuming a Gaussian beam profile, we describe the normalized transversal density distribution by

$$f(x,y)dxdy = \frac{1}{2\pi\sigma_x\sigma_y}\, e^{-x^2/2\sigma_x^2}\, e^{-y^2/2\sigma_y^2} dxdy. \tag{S13}$$

Conversion to polar coordinates r, ϕ yields

$$f(r,\phi)drd\phi = \frac{\sqrt{a_x a_y}}{\pi}\, e^{-r^2(a^+ + a^- \cos 2\phi)} r dr d\phi \tag{S14}$$

TABLE S4. Measured r.m.s. ion beam radii σ_x and σ_y, the deduced overlap ratio $\eta_\perp$, and the effective r.m.s. radii and FWHM diameters of a round ion beam with the same overlap ratio. Estimated standard deviation uncertainties are included.

	$t = 10$ s	$t = 20$ s
σ_x (mm)	2.98(30)	2.40(24)
σ_y (mm)	1.70(17)	1.56(16)
$\eta_\perp$	0.88(4)	0.95(2)
$\hat{\sigma}$ (mm)	2.45(22)	2.07(19)
Effective FWHM diam. (mm)	5.77(52)	4.87(45)

with $a_i = 1/2\sigma_i^2$ for $i = x$ and y, and $a^\pm = (a_x \pm a_y)/2$. The transverse overlap fraction $\eta_\perp$ for an electron beam radius ρ is then

$$\eta_\perp = \sqrt{a_x a_y} \int_0^{\rho^2} e^{-a^+ u}\, I_0(a^- u)\, du, \tag{S15}$$

with the angular integration of Eq. (S14) being equivalent to the integral representation of the modified Bessel function I_0. The integral of Eq. (S15) is easily calculated numerically. Using the measured electron beam diameter [$2\rho = 10.2(5)$ mm, see p. 9] leads to the results for $\eta_\perp$ listed in Table S4. We conclude that the overlap efficiency appropriate to our 50% duty cycle measurement conditions is $\eta_\perp = 0.91(4)$.

For a round beam of r.m.s. radius $\hat{\sigma} = 1/\sqrt{2\hat{a}}$ the overlap fraction would be $\hat{\eta}_\perp = 1 - e^{-\hat{a}\rho^2}$. The $\hat{\sigma}$ that yields $\hat{\eta}_\perp = \eta_\perp$ is

$$\hat{\sigma} = \rho/\sqrt{2\ln[1/(1-\eta_\perp)]}. \tag{S16}$$

The radii $\hat{\sigma}$ and FWHM diameters for an equivalent round ion beam are included in Table S4. They lead to the < 6 mm effective ion beam diameter quoted in the main paper.

For ions circulating in the storage ring, the rate of the collisionally induced process is then

$$R = \eta_\perp (l_0/C_0) n_e \alpha^{\mathrm{mb}}\,. \tag{S17}$$

All results were obtained with the given n_e (see p. 10). The factor linking all collisional rates R to α^{mb} is $\bar{n}_e = \eta_\perp (l_0/C_0) n_e = 2.06(21) \times 10^4$ cm^{-3}, representing the effective average of the electron density over the storage ring circumference.

4. Theoretical results on CH^+ rotationally inelastic collisions

The cross section for rotationally inelastic collisions of electrons with positive molecular ions can be calculated [17, 18] in compact form using the Coulomb–Born (CB) approximation, which assumes

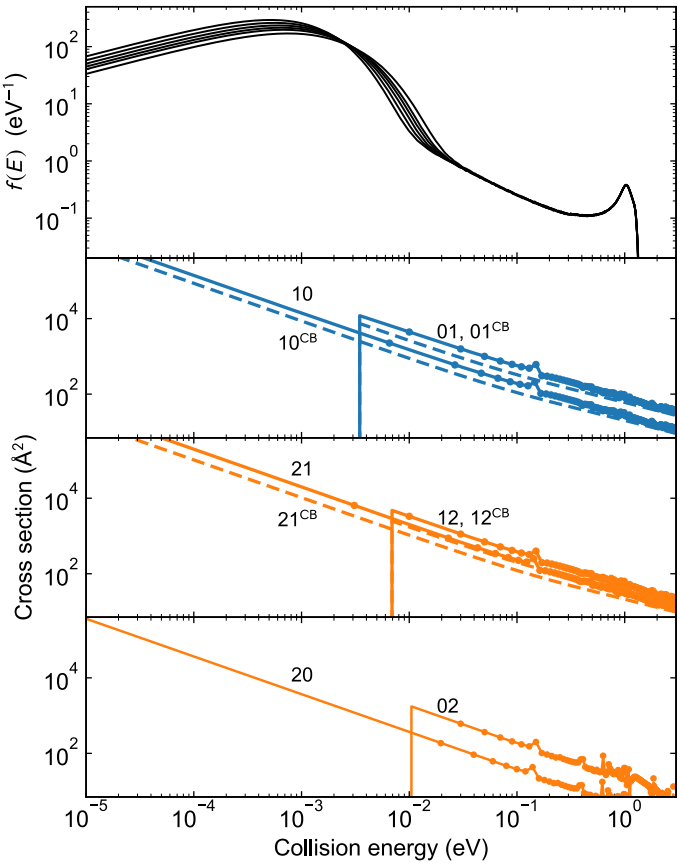

FIG. S5. Upper panel: Modeled merged-beams velocity distributions (normalized) for matched average beam velocities and transverse electron temperatures of $k_B T_\perp$ varying from 1.5 meV to 3 meV (in steps of 0.25 meV from 1.5 to 2.5 meV). Lower panels: Inelastic electron cross sections $\sigma_{J,J'}(E)$ for $J, J' \leq 2$. Dots and full lines with labels JJ': results by Hamilton *et al.* [19] (dots) with interpolation and extrapolation as described in the text. Dashed lines and labels JJ'^{CB}: Coulomb-Born approximation calculated with Eqs. (S18) and (S20).

the free-electron wave functions for a $1/r$ Coulomb potential of the ion and multipole interaction with the molecular charge distribution to be valid at all distances from the molecular center of mass. For free–free transitions of the incident electron leading to molecular excitation, the cross section for electric dipole interaction in first-order perturbation theory is obtained for rotational excitation $J \to J+1$ as

$$\sigma_{J,J+1}(E) = \frac{4\pi^2 a_0^2}{3\sqrt{3}} \frac{E_0}{\Delta E} \left(\frac{\mu_0}{e a_0}\right)^2 \frac{J+1}{2J+1} \frac{\Delta E}{E} g_{ff}(w,\epsilon), \tag{S18}$$

where $E \geq \Delta E$ is the incident electron energy and ΔE the excitation energy, μ_0 the molecular electric dipole moment (in the vibrational ground state for the present case). E_0 and a_0 are the atomic unit of energy and the Bohr radius, respectively. The angular factors apply to rotational levels in a $^1\Sigma^+$ electronic state. The Gaunt factor $g_{ff}(w,\epsilon)$ represents the integral over the continuum Coulomb wave functions with the parameters $w = 2\Delta E/E_0$ and $\epsilon = 2(E-\Delta E)/E_0$. We interpolate $g_{ff}(w,\epsilon)$

from the recent high-accuracy tabulation by van Hoof *et al.* [20]. The Gaunt factors near threshold ($\epsilon \ll w$) are close to 1 and significantly vary only for $\epsilon \gg w$. Hence, Eq. (S18) implies that $\sigma_{J,J+1}$ abruptly rises to $\sigma_0^{J,J+1}$ at $E = \Delta E$ and, at higher E, decreases approximately proportional to $1/E$.

The CB expression Eq. (S18) is also suitable for estimating vibrational excitation. The related excitation cross section for $v \to v+1$ in the harmonic approximation, after summing over rotational final states, is obtained [17] by replacing

$$\left(\frac{\mu_0}{ea_0}\right)^2 \frac{J+1}{2J+1} \to \left(\frac{\sigma_0}{ea_0}\frac{\partial\mu_0}{\partial R}\bigg|_{r_e}\right)^2 \tag{S19}$$

with the dipole moment derivative at the equilibrium distance r_e (where $\sigma_0 = \sqrt{\hbar/4\pi c\,\omega_e m_r}$, with the reduced mass m_r, is the root-mean-square spatial extension of the vibrational ground-state probability distribution), using also the appropriate excitation energy ΔE. The increasing ΔE and the mostly smaller size of the dipole moment expression in general lead to a significantly smaller excitation cross section for vibration than for rotation.

The significant deviations expected from the assumptions of the CB approximation in the inner molecular region were considered for rotational excitation in recent R-matrix calculations for a number of small diatomic molecules, including CH^+ [19]. Excitation cross section data underlying the rate coefficients presented in Ref. [19] were made available to us by the authors. They are given on an electron energy grid from 0.01 eV in steps of 0.02 eV, thus starting somewhat above the $J = 0$ to 1 threshold (0.00346 eV). Using the cross-section data on this rather coarse energy grid, we determine intermediate values by linear interpolation on a double-logarithmic scale (thus requiring a constant power law between any two points). Moreover, from the lowest grid point above the threshold we extrapolate down in E using the power law of the next-higher interpolation interval.

Inelastic electron-impact cross sections for CH^+ based on Eq. (S18) and on the calculations by Hamilton *et al.* [19] are shown in Fig. S5. In addition to excitation cross sections $\sigma_{J,J+1}(E)$, the de-excitation cross sections $\sigma_{J+1,J}(E)$ are also shown, which for a given pair of levels can be obtained using the principle of detailed balance,

$$g(J+1)\,E\,\sigma_{J+1,J}(E) = g(J)\,(E+\Delta E)\,\sigma_{J,J+1}(E+\Delta E) \tag{S20}$$

where $g(J) = 2J+1$ are the statistical weights of the bound molecular levels. The R-matrix results in Fig. S5 show very similar trends as the compact CB results, with the difference essentially consisting in the value of the excitation cross section at threshold, $\sigma_{J,J+1}(\Delta E) = \sigma_0^{J,J+1}$. Moreover, the CB results follow the dipole selection rule of $|\Delta J| = 1$, while the R-matrix calculations show significant contributions also for $|\Delta J| > 1$. In the present context we consider $J \le 3$ including the R-matrix results with $|\Delta J| \le 3$.

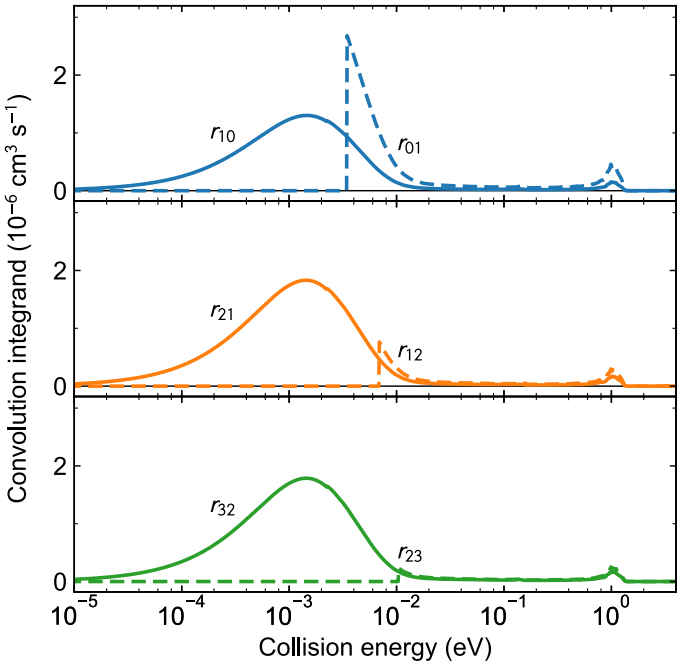

FIG. S6. Logarithmic convolution integrand $r_{J,J'}$ to base $a = 10$ from Eq. (S22) for the rate coefficient calculation of Eq. (S25) using the product of the modeled electron energy distribution ($k_B T_\perp = 2.25$ meV) and the cross sections of Ref. [19] for cooling (full lines) and excitation (broken lines).

The experimental collision energy distributions $f(E)$ shown in the top frame of Fig. S5 suggest that, while de-excitation will be dominant, also excitation will occur and sensitively depend on the transverse electron temperature.

The rates $R_{J,J'}$ of inelastic transitions $J \to J'$ are obtained from the merged-beams rate coefficients $\alpha^{\rm mb}_{J,J'}$ according to Eq. (S12), using the energy distribution $f(E)$ for matched average electron and ion beam velocities and the cross sections $\sigma_{J,J'}(E)$. To illustrate the relevance of the various electron energies, we consider equally spaced bins on a logarithmic energy scale such that, for $x = \log_a E$ to a base a,

$$\alpha^{\rm mb}_{J,J'} = \int_{-\infty}^{\infty} r_{J,J'}(x)\, dx \ . \tag{S21}$$

With $x \ln a = \ln E$ and $dE = E(\ln a)dx$ we obtain the integrand

$$r_{J,J'}(x) = \ln a \, \sqrt{\frac{2}{m}}\, E^{3/2} f(E)\sigma(E) \ . \tag{S22}$$

The energy dependent contributions to the logarithmic integral Eq. (S21) can be visualized directly through the graphical area under the functions $r_{J,J'}$ when plotted with the logarithmic energy scale. They are presented in Fig. S6 for the dipole-allowed excitation and de-excitation channels with the lowest J.

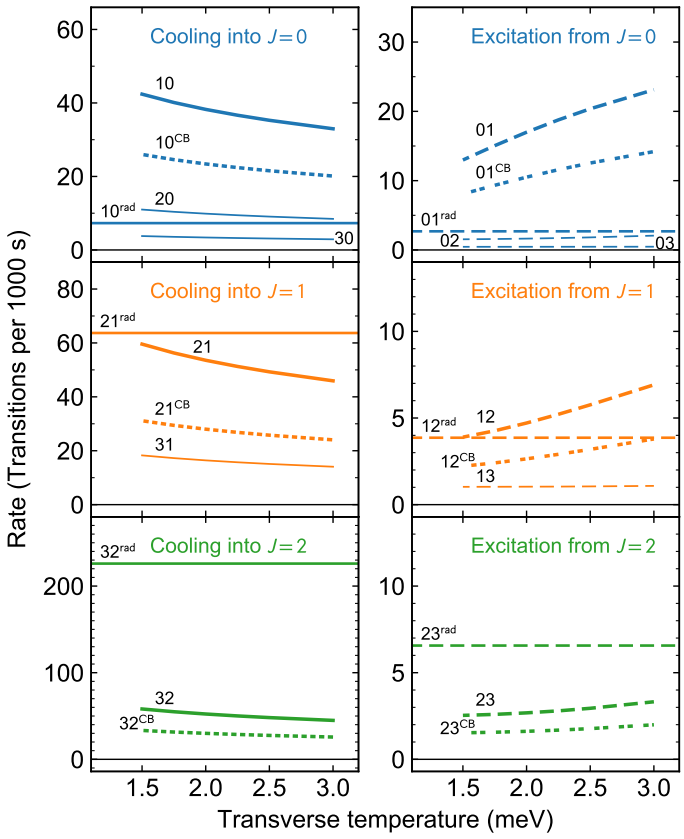

FIG. S7. Modeled rates $R_{J,J'}$ (units of 10^{-3} s^{-1}) for cooling into and excitation from low-J levels as indicated, using the experimental parameters with Eqs. (S17) and (S25). The dependence on the transverse electron temperature $k_B T_\perp$ is shown. Results for the cross section of Ref. [19] (full and long-dashed curves, labels JJ') and for the CB cross sections (short-dashed curves, labels $JJ'^{\rm CB}$). The collisional rates are calculated as $R_{J,J'} = \bar{n}_e \alpha^{\rm mb}_{J,J'}$ setting the ring-averaged electron density to $\bar{n}_e = 2.06 \times 10^4$ cm^{-3}. Also included are the radiative cooling and excitation rates from Eqs. (S3) and (S4) (horizontal full and dashed lines; labels $JJ'^{\rm rad}$). Note the scale change for the cooling rates as J increases.

The numerical integration makes use of the exponential decrease of $r_{J,J'}(x)$ at high energy and can be performed conveniently from the sum over bins on a fine grid in x. At low energy ($x \to -\infty$) both, $f(E)$ and $\sigma_{J,J'}(E)$, remain finite for the cooling channels ($J' < J$). Here we extend the explicit calculation of $r_{J,J'}$ down to a limit $\epsilon \ll k_B T_\perp, k_B T_{||}$ so that for $E < \epsilon$ the energy distribution and the cross sections are well approximated by

$$f(E) = \sqrt{\frac{E}{\epsilon}}\, f(\epsilon) \quad \text{and} \quad \sigma_{J,J'}(E) = \frac{\epsilon}{E}\, \sigma_{J,J'}(\epsilon)\,. \tag{S23}$$

With $x_0 = \log_a \epsilon$ this implies for $x < x_0$

$$r_{J,J'}(x) = \sqrt{\frac{2}{m}}\, \epsilon^{3/2} f(\epsilon) \sigma_{J,J'}(\epsilon)\, \frac{E}{\epsilon} = r_{J,J'}(x_0)\, e^{(x-x_0)\ln a} \tag{S24}$$

such that Eq. (S21) can be replaced by

$$\alpha^{\mathrm{mb}}_{J,J'} = \frac{r_{J,J'}(x_0)}{\ln a} + \int_{x_0}^{\infty} r_{J,J'}(x)dx \ . \tag{S25}$$

The chosen limit ϵ corresponds to the lowest value on the logarithmic scale shown in Fig. S6.

The inelastic rates $R_{J,J'}$ for our experimental conditions are obtained according to Eq. (S17) by multiplication of $\alpha^{\mathrm{mb}}_{J,J'}$ with the fixed ring-averaged electron density, for which we here assume the value of $\bar{n}_e = 2.06 \times 10^4$ cm^{-3}. The results are shown in Fig. S7 for the estimated experimental range of the transverse electron temperature $T_\perp$ discussed above.

For comparison, Fig. S7 includes also the radiative transition rates for rotational cooling and excitation from Eqs. (S3) and (S4). It can be seen that the additional effect of inelastic electron collisions is expected to substantially exceed the radiative rates for the transitions between the rotational ground state and the $J = 1$ excited state. Thus, the time constant (reciprocal rate) is 141 s for radiative cooling $J = 1 \to J' = 0$ [at the fitted CSR effective occupation number, Eq. (S5)] and is expected to become ~ 25 s through inelastic electron collisions. Between the levels $J = 2$ and 1, electronic and radiative rates are of similar size for both cooling and excitation, while for the level pair $J = 3$ and 2 the electronic rates are small compared to radiational cooling and excitation. Note that the collisional cooling rates keep their magnitude for higher J, while the radiative cooling rates rapidly increase with J. For the comparison with the experimental results, we consider that rotational levels $J \geq 3$ will have relaxed radiatively after > 10 s of storage and neglect their population at later times. The rotational population model is hence restricted to the three levels $J \leq 2$.

5. Time dependent modeling

The relative rotational populations in the stored beam are defined as $p_J = N_J/N$ where $N = \sum_J N_J = N_i$ is the total number of stored ions. We consider total rates $a_{JJ'}$ leading to transitions $J \to J'$, which conserve the N. The master equation for the relative populations is given by

$$\dot{p}_J = \sum_{J'} a_{J'J}\, p_{J'} - p_J \sum_{J'} a_{JJ'} \tag{S26}$$

where

$$a_{JJ'} = \delta_{J',J-1}\, k^{\mathrm{em}}_{J\to J-1} + \delta_{J',J+1}\, k^{\mathrm{abs}}_{J\to J+1} + R_{JJ'}. \tag{S27}$$

with the radiative rates from Eqs. (S3) and (S4) and the inelastic collision rates $R_{JJ'}$ as presented in Fig. S7. ($\delta_{i,j}$ denotes the Kronecker delta.)

The equilibrium populations $p_{J,\mathrm{eq}}$ follow from setting $\dot{p}_J = 0$ in Eq. (S26). Considering radiation only ($R_{JJ'} = 0$), Eqs. (S3), (S4) and (S27) lead for the equilibrium population ratio of two subsequent

rotational levels to

$$(p_{J+1}/p_J)_{\rm eq} = \frac{2J+3}{2J+1}\,\frac{n(\tilde{\nu}_J)}{1+n(\tilde{\nu}_J)}. \tag{S28}$$

Assuming a fully thermal radiation field, i.e., $n(\tilde{\nu}_J) = n_{\rm th}(\tilde{\nu}_J, T_r^{\rm eff})$ according to Eq. (S2) with an effective temperature $T_r^{\rm eff}$, results for $J = 0$ in

$$(p_1/p_0)_{\rm eq} = 3e^{-hc\tilde{\nu}_0/k_B T_r^{\rm eff}} \quad \Rightarrow \quad T_r^{\rm eff} = -\frac{hc\tilde{\nu}_0}{k_B}\frac{1}{\ln[(1/3)(p_1/p_0)_{\rm eq}]}. \tag{S29}$$

This is used to derive $T_r^{\rm eff}$ in the main paper.

Changes of the relative rotational populations can also be caused by the DR in merged-beams collisions at matched electron and ion velocities, according to the level-dependent loss rates $r_J = -\dot{N}_J/N$. As these collisions lead to a change in the total ion number N, the effect on p_J is described by the non-linear equation

$$(\dot{p}_J)_{\rm DR} = \left(\sum_{J'} r_{J'}\, p_{J'} - r_J\right) p_J \tag{S30}$$

which follows from $\dot{p}_J = (d/dt)(N_J/N)$, considering the time derivatives of both N_J and $N = \sum_J N_J$. We explicitly consider Eq. (S30) in the model used for Fig. 3 of the main paper. For the purpose of a rough estimate, consider the rate of population change in a two-level system ($J = 0$ and 1) with $p_0 = p_1 = \frac{1}{2}$. Eq. (S30) then leads to

$$\begin{aligned}(\dot{p}_0)_{\rm DR} &= \tfrac{1}{4}(r_1 - r_0) = \tfrac{1}{2}(r_1 - r_0)p_0 \\ (\dot{p}_1)_{\rm DR} &= \tfrac{1}{4}(r_0 - r_1) = \tfrac{1}{2}(r_0 - r_1)p_1\ .\end{aligned} \tag{S31}$$

The result of this estimate is given in Supplemental Sec. 8.

6. Constraining the transverse temperature

The uncertainty of $T_\perp$ translates into an uncertainty of the modeled inelastic rates. Since we measure the rotational populations for up to 150 s, while the expected total cooling time constants $(1/R)$ amount to at most 25 s (see Fig. S7), the longest storage time should already come close to the collisional equilibrium populations. The rotational levels most sensitive to this equilibrium are $J = 0$ and 1. We have calculated time-dependent models of p_J for a set of discrete values of $k_B T_\perp$ in the estimated experimental range (see Fig. S8) and compare these results to the populations measured by laser probing. The best agreement of the modeled $p_{0,1}$ with the measurement in the final probing interval ($t = 141$ s) is obtained for the model with $k_B T_\perp = 2.25$ meV. From this we conclude the experimentally constrained value of $k_B T_\perp = 2.25(25)$ meV used in the main paper.

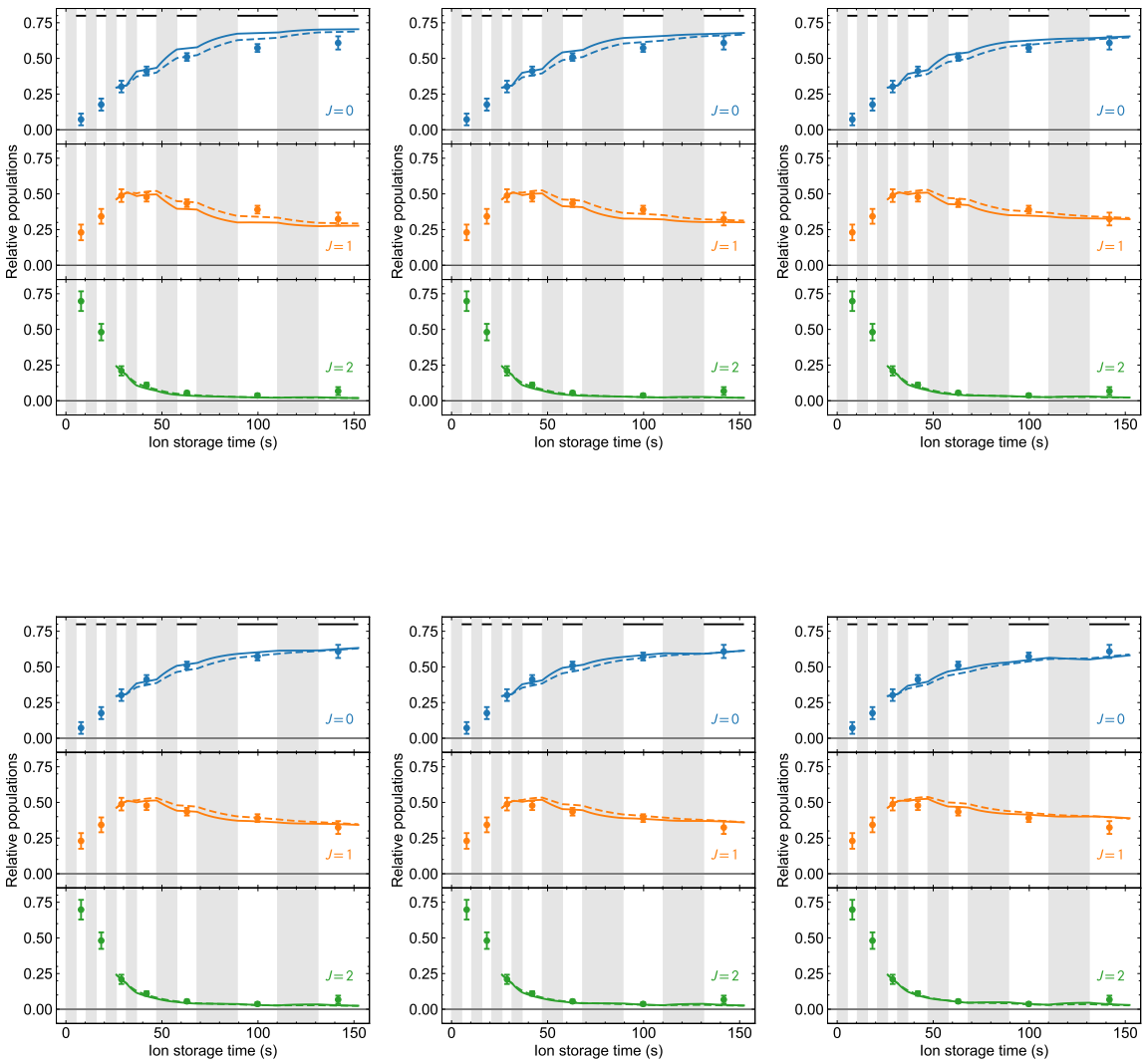

FIG. S8. Modeled relative rotational populations $p_J(t)$ for the complete rate-equation model as described in the main paper for the following transverse temperatures: upper row, left to right, $k_B T_\perp = 1.5, 1.75, 2.0$ meV; lower row, left to right, $k_B T_\perp = 2.25, 2.5, 3.0$ meV. As in the main paper, the rate-model results from the CB approximation and the R-matrix calculations [19] are shown by dashed and full curves, respectively.

7. Metastable electronically excited CH^+ state

The excitation of the metastable $a\,^3\Pi$ electronic state in the stored ion beam is revealed by the KER of the neutral DR products observed at the MCP. The $1\sigma^2 2\sigma^2 3\sigma^2\ X^1\Sigma^+$ ground state of CH^+ lies ~7.18 eV above the lowest neutral level $C(2s^2 2p^2\ ^3P) + H(1s)$. In DR at near-zero electron collision energy (matched beam velocities) the mainly populated final state is $C(2s^2 2p^2\ ^1D) + H(1s)$ with a

KER close to 5.9 eV. Higher excited singlet and triplet terms, starting at 7.48 eV with C($2s^2 2p 3s\ ^3P$), cannot be reached from the CH^+ ground state. Conversely, the lowest triplet state $1\sigma^2 2\sigma^2 3\sigma 1\pi\ a\,^3\Pi$ of CH^+ lies ∼1.18 eV above $CH^+(X\,^1\Sigma^+)$. Hence, DR of low-energy electrons with the metastable CH^+ ions can reach such higher excited terms. The C($2s2p^3\ ^3D$) term (7.95 eV above the C ground state) is found here (as earlier by Amitay *et al.* [9]) to be by far the dominating channel for low-energy DR of $CH^+(a\,^3\Pi)$. The KER, whose value identifies the final as well as the initial levels of the DR process, is near 0.4 eV, much lower than that for the CH^+ ground state. DR events with higher KER, and thus lower lying terms of the C atom as final channels, were not detected from metastable CH^+ ions.

We follow the earlier procedure [9] and extract the relative DR signals (at matched beam velocities) from the $X\,^1\Sigma^+$ (S_g) and $a\,^3\Pi$ (S_m) states by analyzing the magnitude of the contribution with low KER, assigned to the metastable state, to the observed DR-product imaging distribution as a function of storage time. Assuming a constant ratio of the effective (i.e., J-averaged) DR cross sections for the metastable σ_m and the ground states σ_g, the ratio of these DR signals can be expressed in terms of the relative metastable population $\hat{p}_m(t)$ as

$$R\,(t) = \frac{S_\mathrm{m}}{S_\mathrm{g}} = \frac{\sigma_\mathrm{m}}{\sigma_\mathrm{g}} \frac{\hat{p}_m(t)}{1-\hat{p}_m(t)}. \tag{S32}$$

The storage times for the present data extend up to 100 s while they were limited to 25 s in the previous measurements [9]. Starting at the times of ∼ 3 s after injection, we can account for the $R(t)$ data (see Fig. S9) by assuming a single-exponential model for $\hat{p}_m(t)$

$$\hat{p}_m(t) = \hat{p}_{m,t_0}\, e^{-(t-t_0)/\tau_m} + \hat{p}_{m,\infty} \tag{S33}$$

with an exponential decay [$\tau_m = (10.1 \pm 1.0)$ s and $\hat{p}_{m,t_0} = (0.10 \pm 0.03)$ for $t_0 = 21\,\mathrm{s}$] and constant offset [$\hat{p}_{m,\infty} = (0.025 \pm 0.007)$]. Around the start of the observation, this fitted $\hat{p}_m(t)$ amounts to more than 0.4. This causes the relation of $R(t)$ to $\hat{p}_m(t)$ to be significantly non-linear, such that we can independently fit both $\sigma_\mathrm{m}/\sigma_\mathrm{g} = 0.8 \pm 0.3$ and the $\hat{p}_m(t)$ model parameters. A probable candidate as the source of the long-lived (≫ 100 s) $a\,^3\Pi$ contribution signal can be attributed to the $a\,^3\Pi(v = 0, J = 0, f$ symmetry) sublevel. The existence of this longer lived metastable rotational level was pointed out earlier [4], predicting that it can radiatively decay only via much slower *magnetic* dipole transitions (mean lifetimes ≫ 100 s).

We find a lifetime τ_m somewhat longer than the previous value [9] of (7 ± 1) s, which we explain by the extended time range of the measurement, our different cooling conditions for the rotational populations, and the modified fit model including a longlived contribution. We consider the fit results using Eq. S33 as the best estimate of the metastable population and apply it for the analysis of the DR

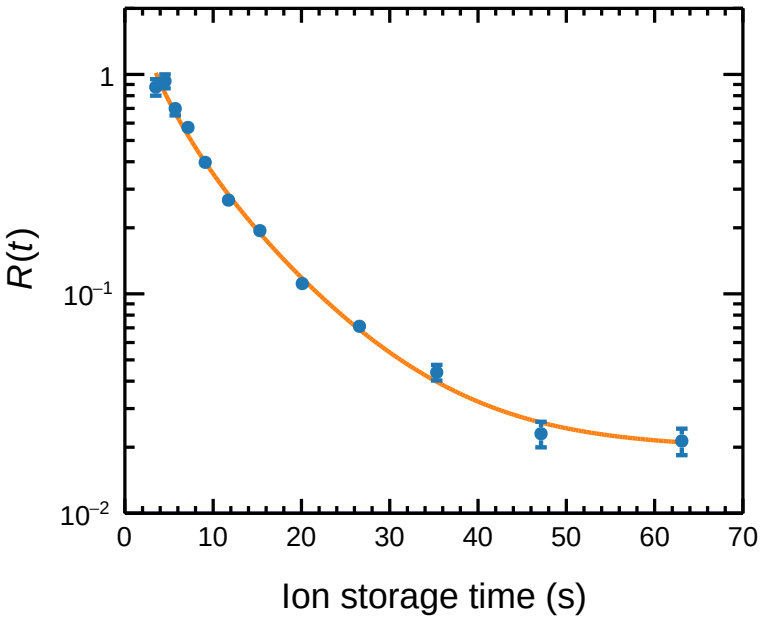

FIG. S9. Metastable state characterization from DR-product imaging. The observed relative contribution of low-KER DR signal $R(t)$ as a function of storage time is given by the symbols with 1σ statistical errorbars. Full line: fit of the data using Eq. S32 and the metastable population model of Eq. S33.

rates in Supplement Sec. 8. Regarding possible feeding of J-levels in the ground state by metastable decays, this is equivalent to the fractional metastable populations $\hat{p}_m < 0.1$ for $t > 25\,\mathrm{s}$ and < 0.05 for $t > 40\,\mathrm{s}$ as stated in the main paper. Considering faster earlier decay components in a more complex model of $\hat{p}_m(t)$ would imply smaller non-linear effects in the function $\hat{p}_m(t)/(1-\hat{p}_m(t))$, which after fitting the parameters would lead to even lower values for $\hat{p}_{m,t_0}$ and to larger values of $\sigma_\mathrm{m}/\sigma_\mathrm{g}$. As for the assumption of a constant ratio of $\sigma_\mathrm{m}/\sigma_\mathrm{g}$ in the observed time window, we examined the underlying mechanism that drives DR for the metastable state. For the DR from ground-state CH^+, we observe a weak rotational dependence among the relevant low-J levels (see Supplement Sec. 8, Table S5). Theoretically, such a weak dependence is predicted [21] for a strong neutral dissociating resonance for low-energy electronic continuum states with the CH^+ core, which manifests itself in an anti-crossing pattern within the energetic structure of the $^2\Pi$ Rydberg states of CH (see Fig. 1 of Ref. [22]). A similar efficient direct DR route likely also exists for the $a\,^3\Pi$ metastable state of CH^+, considering the energetic structure in the Rydberg states of $^2\Sigma^-$ and $^2\Delta$ symmetries of CH (see Fig. 3 of Ref. [22]). Given the non-resonant nature of such a direct DR pathway, only a weak rotational dependence for the DR rate coefficient [23] is likely expected for metastable ($a\,^3\Pi$) CH^+.

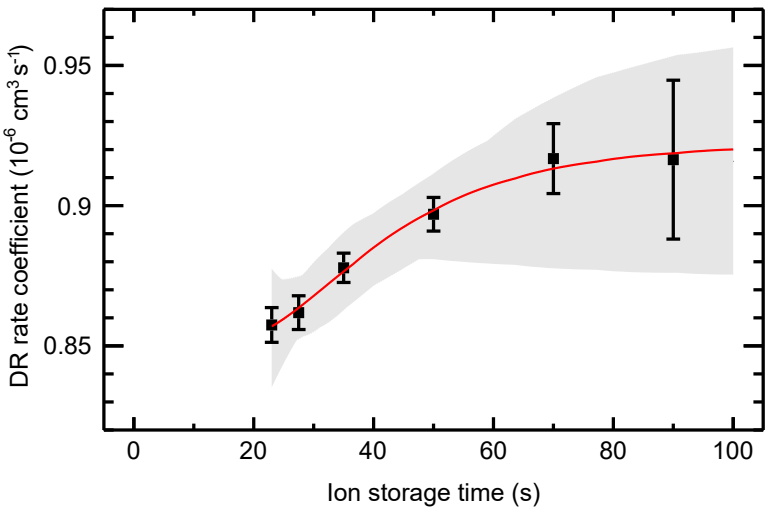

FIG. S10. Total DR rate coefficient storage time dependence. Black symbols: measured values and 1σ statistical uncertainty; red line: time dependence from the model of Eq. (S34) using the best estimator values for α_J and α_m from the MCMC analysis; gray area: space covered by all parameter combinations sampled in the MCMC analysis.

8. Rotational dependence of dissociative recombination

The laser probing was also combined with studies of the DR rate. Laser probing and DR measurements could in general not be performed simultaneously, as laser probing required high stored ion numbers (typically 10^7 ions) to observe sufficient photodissociation signal with the pulsed laser, while the continuous count rates from DR had to be limited by lower stored ion numbers (typically 10^6 ions) to avoid saturation of the detector. However, a control cycle was developed where the electron velocity was repeatedly set (in a wobbling scheme with typical dwell times of 30 ms) to values detuned from the ion beam velocity. Velocity-detuned time windows were used to measure the background in the detector count rate not induced by electron collisions (subtracted for determining the DR merged-beams rate coefficient) and for laser probing to find the time dependent relative rotational populations. This way, laser-probing and DR measurements were performed for the same control cycle such that the effect of changing, laser-probed rotational populations on the DR rate coefficient could be analyzed. To distinguish the relative populations from those discussed in the main paper (measured while only matched electron and ion beam velocities were used) they are denoted as $\hat{p}_J$ in the following. The given DR rate coefficients always refer to those measured in the wobbling phases when the average electron and ion beam velocities were matched to each other.

As shown in Fig. S10, the DR rate at matched average beam velocities (corresponding to the present laser probing of inelastic collisions) showed a slight time dependence that is attributed to

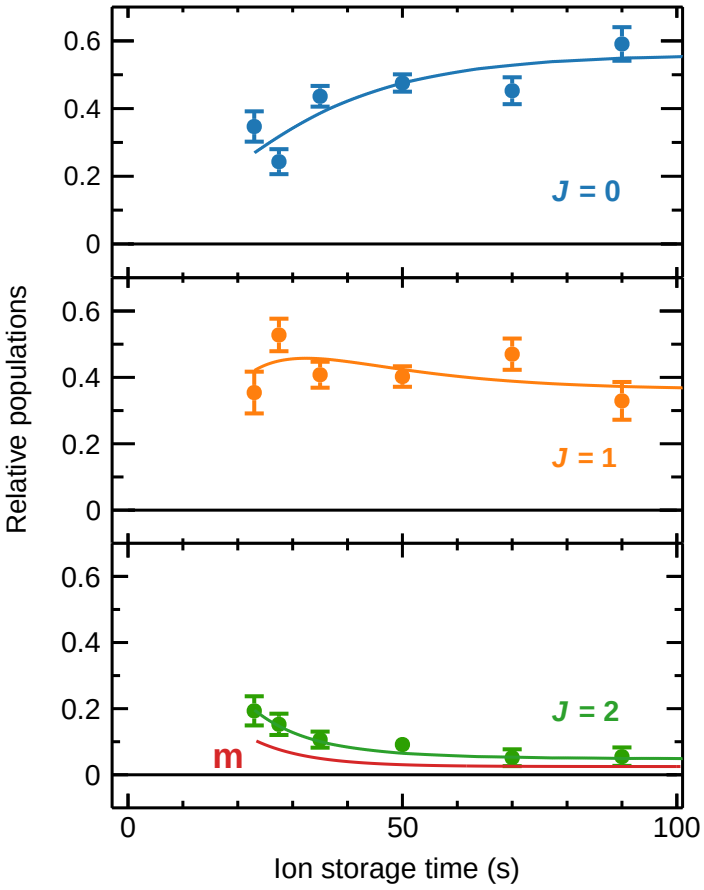

FIG. S11. Relative populations $\hat{p}_J(t)$, $J = 0 \ldots 2$, determined from laser probing measurements performed with the same control cycle for the electron beam intensity and energy as in the DR rate measurements, but with increased stored ion number. Smooth lines were added to the panels, which were drawn to best represent the observed storage time evolution. The metastable $a\,^3\Pi$ state population $\hat{p}_m(t)$ (Eq. S33) is displayed in the bottom panel.

the variation of the relative populations $\hat{p}_J(t)$ of the three lowest levels $J = 0 \ldots 2$. We assume for these levels DR rate coefficients α_J [corresponding to the quantities $\alpha_{\rm DR}^{\rm mb}(J)$ used in the main paper; $\alpha_J = \alpha_{\rm DR}^{\rm mb}(J)$] as well as α_m for the $a\,^3\Pi$ state (see Sec. 7 of this Supplemental Information). With this we model the total DR rate by

$$\alpha(t) = \sum_{J=0}^{2} \alpha_J \hat{p}_J(t) + \alpha_m \hat{p}_m(t) \tag{S34}$$

where the populations $\hat{p}_J(t)$ are normalized such that their sum amounts to $1 - \hat{p}_m(t)$ [see Eq. (S33)].

The laser-probed rotational populations are visualized in Fig. S11. Within the statistical scatter, the data for $J = 0$ and $J = 2$ show clear trends in $\hat{p}_J(t)$ that should lead to changes in $\alpha(t)$ depending on the J-dependence of the DR rate coefficients. We represent the trends in $\hat{p}_J(t)$ by smooth curves with normalized relative populations, which is included in Fig. S11.

TABLE S5. Level-specific DR rate coefficients $\alpha_J = \alpha_{\rm DR}^{\rm mb}(J)$ $(J = 0 \ldots 2)$ and α_m of CH^+ in the merged beams at matched average beam velocities as determined from the MCMC analysis. The limits given are the estimated 1σ uncertainties of the fitted results except for α_2 and α_m where both limits are sharp corresponding to the positive parameter values required in the MCMC sampling.

Quantity	Value (10^{-6} cm^3 s^{-1})
α_0	1.053 ± 0.062
α_1	0.741 ± 0.083
α_2	0.8 ± 0.8
α_m	1.4 ± 1.4
$\bar{\alpha}_{01} = (\alpha_0 + \alpha_1)/2$	0.897 ± 0.015
$\alpha_0 - \alpha_1$	0.31 ± 0.15

To estimate the parameters α_J and α_m in the model of Eq. (S34) we use the smoothed trends of $\hat{p}_J$. A linear least-squares minimization procedure cannot be applied in our case since its results violate the physical constraints $\alpha_J > 0$ and $\alpha_m > 0$. Thus, we use the more robust Markov-chain Monte-Carlo (MCMC) analysis method [24]. The latter is based on the Bayesian inference principle and samples the marginal-likelihood function of the model over the relevant parameter space with Markov chains, i.e., in a more efficient way than sampling uniformly. As a result, the MCMC analysis provides the probability distributions for all parameters, i.e., α_J and α_m, and their mutual correlations.

We use the MCMC package EMCEE [25] and constrain the valid parameter space to positive values for all rate coefficients. As a prior we choose for all parameters a broad uniform distribution over the interval $[0, 1] \times 10^{-5}$ cm^3 s^{-1}. After $\sim$60 iterations the MCMC routine converges and a further 10^5 iterations are used to generate the aforementioned probability distributions for the individual rate coefficients α_J and α_m and specific linear combinations. From those, the most probable values and the uncertainties of the parameters are derived as mean values and standard deviations of the distributions for α_0 and α_1 (with sharp uncertainties given from the extent of the distributions for α_2 and α_m), as summarized in Table S5. The results document that the average $\bar{\alpha}_{01}$ of the $J = 0$ and 1 rate coefficients is found with a smaller relative uncertainty than the difference $\alpha_0 - \alpha_1$. To calculate the effect of the J-specific DR rates on the populations according to Eq. (S30), we use $r_j = \bar{n}_e \alpha_{\rm DR}^{\rm mb}(J)$ with the best estimator values given for $\alpha_J = \alpha_{\rm DR}^{\rm mb}(J)$ in Table S5. The results of this time dependent model are shown in Fig. 3 of the main paper.

We remark that the experimental result for $\alpha_0 - \alpha_1$ (Table S5), the ring-averaged electron density, and the estimate of effects caused by J-specific DR at the end of Supplemental Sec. 5, Eq. (S31), lead

to $(\dot{p}_0/p_0)_{\rm DR} \approx -(\dot{p}_1/p_1)_{\rm DR} \approx -(3.2 \pm 1.5) \times 10^{-3}$ s^{-1}. This estimate can be directly compared to the inelastic and radiative rates shown in Fig. S7. The effect of the J-specific DR rates counteracts the increase of p_0 due to the radiative cooling. Its magnitude corresponds to only about half the $J = 1 \rightarrow 0$ cooling rate $k^{\rm em}_{1\rightarrow 0}$ included in this figure (label $10^{\rm rad}$). However, the DR-induced J-changing rates are about an order of magnitude lower than those caused by the inelastic collisions.

[1] U. Hechtfischer, C. J. Williams, M. Lange, J. Linkemann, D. Schwalm, R. Wester, A. Wolf, and D. Zajfman, Photodissociation spectroscopy of stored CH^+ ions: Detection, assignment, and close-coupled modeling of near-threshold Feshbach resonances, J. Chem. Phys. **117**, 8754 (2002).

[2] P. F. Bernath, *Spectra of Atoms and Molecules*, 2nd ed. (Oxford University Press, New York, 2005).

[3] R. Hakalla, R. Kępa, W. Szajna, and M. Zachwieja, New analysis of the Douglas-Herzberg system ($A^1\Pi$-$X^1\Sigma^+$) in the CH^+ ion radical, Eur. Phys. J. D **38**, 481 (2006).

[4] U. Hechtfischer, J. Rostas, M. Lange, J. Linkemann, D. Schwalm, R. Wester, A. Wolf, and D. Zajfman, Photodissociation spectroscopy of stored CH^+ and CD^+ ions: Analysis of the $b^3\Sigma^-$–$a^3\Pi$ system, J. Chem. Phys. **127**, 204304 (2007).

[5] I. Kusunoki and C. Ottinger, Triplet $CH^+(CD^+)$ emission from chemiluminescent ion–molecule reaction $C^+(^4P)$+ $H_2(D_2)$, J. Chem. Phys. **73**, 2069 (1980).

[6] J. L. Doménech, P. Jusko, S. Schlemmer, and O. Asvany, The first laboratory detection of vibration-rotation transitions of $^{12}CH^+$ and $^{13}CH^+$ and improved measurement of their rotational transition frequencies, Astrophys. J. **857**, 61 (2018).

[7] C. Meyer, A. Becker, K. Blaum, C. Breitenfeldt, S. George, J. Göck, M. Grieser, F. Grussie, E. Guerin, R. von Hahn, P. Herwig, C. Krantz, H. Kreckel, J. Lion, S. Lohmann, P. Mishra, O. Novotný, A. O'Connor, R. Repnow, S. Saurabh, D. Schwalm, L. Schweikhard, K. Spruck, S. Sunil Kumar, S. Vogel, and A. Wolf, Radiative rotational lifetimes and state-resolved relative detachment cross sections from photodetachment thermometry of molecular anions in a cryogenic storage ring, Phys. Rev. Lett. **119**, 023202 (2017).

[8] M. Cheng, J. M. Brown, P. Rosmus, R. Linguerri, N. Komiha, and E. G. Myers, Dipole moments and orientation polarizabilities of diatomic molecular ions for precision atomic mass measurement, Phys. Rev. A **75**, 012502 (2007).

[9] Z. Amitay, D. Zajfman, P. Forck, U. Hechtfischer, B. Seidel, M. Grieser, D. Habs, R. Repnow, D. Schwalm, and A. Wolf, Dissociative recombination of CH^+: Cross section and final states, Phys. Rev. A **54**, 4032 (1996).

[10] A. O'Connor, A. Becker, K. Blaum, C. Breitenfeldt, S. George, J. Göck, M. Grieser, F. Grussie, E. Guerin, R. von Hahn, U. Hechtfischer, P. Herwig, J. Karthein, C. Krantz, H. Kreckel, S. Lohmann, C. Meyer, P. Mishra, O. Novotný, R. Repnow, S. Saurabh, D. Schwalm, K. Spruck, S. Sunil Kumar, S. Vogel, and A. Wolf, Photodissociation of an internally cold beam of CH^+ ions in a cryogenic storage ring, Phys. Rev. Lett. **116**, 113002 (2016).

[11] Ğ. Barinovs and M. C. van Hemert, CH^+ potential energy curves and photodissociation cross-section, Chem. Phys. Lett. **399**, 406 (2004).

[12] D. A. Orlov, U. Weigel, M. Hoppe, D. Schwalm, A. S. Jaroshevich, A. S. Terekhov, and A. Wolf, Cold electrons from cryogenic GaAs photocathodes: Energetic and angular distributions, Hyperfine Interact. **146/147**, 215 (2003).

[13] S. Pastuszka, U. Schramm, M. Grieser, C. Broude, R. Grimm, D. Habs, J. Kenntner, H.-J. Miesner, T. Schüßler, D. Schwalm, and A. Wolf, Electron cooling and recombination experiments with an adiabatically expanded electron beam, Nucl. Instrum. Methods Phys. Res. Sect. A – Accel. Spectrom. Dect. Assoc. Equip. **369**, 11 (1996).

[14] G. I. Budker and A. N. Skrinskiĭ, Electron cooling and new possibilities in elementary particle physics, Usp. Fiz. Nauk **124**, 561–595 (1978) [Sov. Phys. Usp. **21**, 277–296 (1986)].

[15] C. Krantz, H. Buhr, M. Grieser, M. Lestinsky, O. Novotný, S. Novotny, D. Orlov, R. Repnow, A. Terekhov, P. Wilhelm, and A. Wolf, Transverse electron cooling of heavy molecular ions, Phys. Rev. Accel. Beams **24**, 050101 (2021).

[16] R. von Hahn, A. Becker, F. Berg, K. Blaum, C. Breitenfeldt, H. Fadil, F. Fellenberger, M. Froese, S. George, J. Göck, M. Grieser, F. Grussie, E. A. Guerin, O. Heber, P. Herwig, J. Karthein, C. Krantz, H. Kreckel, M. Lange, F. Laux, S. Lohmann, S. Menk, C. Meyer, P. M. Mishra, O. Novotný, A. P. O'Connor, D. A. Orlov, M. L. Rappaport, R. Repnow, S. Saurabh, S. Schippers, C. D. Schröter, D. Schwalm, L. Schweikhard, T. Sieber, A. Shornikov, K. Spruck, S. Sunil Kumar, J. Ullrich, X. Urbain, S. Vogel, P. Wilhelm, A. Wolf, and D. Zajfman, The cryogenic storage ring CSR, Rev. Sci. Instrum. **87**, 063115 (2016).

[17] R. F. Boĭkova and V. D. Ob''edkov, Rotational and vibrational excitation of molecular ions by electrons, Zh. Eksp. Teor. Fiz. **54**, 1439 (1968) [Sov. Phys. JETP **27**, 772–774 (1968)].

[18] D. A. Neufeld and A. Dalgarno, Electron-impact excitation of molecular ions, Phys. Rev. A **40**, 633 (1989).

[19] J. R. Hamilton, A. Faure, and J. Tennyson, Electron-impact excitation of diatomic hydride cations – I. HeH^+, CH^+, ArH^+, Mon. Not. R. Astron. Soc. **455**, 3281 (2016).

[20] P. A. M. van Hoof, R. J. R. Williams, K. Volk, M. Chatzikos, G. J. Ferland, M. Lykins, R. L. Porter, and Y. Wang, Accurate determination of the free–free Gaunt factor – I. Non-relativistic Gaunt factors, Mon. Not. R. Astron. Soc. **444**, 420 (2014).

[21] Z. J. Mezei, M. D. Epée Epée, O. Motapon, and I. F. Schneider, Dissociative recombination of CH^+ molecular ion induced by very low energy electrons, Atoms **7**, 82 (2019).

[22] G. J. Vázquez, J. M. Amero, H. P. Liebermann, R. J. Buenker, and H. Lefebvre-Brion, Insight into the Rydberg states of CH, J. Chem. Phys. **126**, 164302 (2007).

[23] M. Larsson and A. E. Orel, *Dissociative Recombination of Molecular Ions* (Cambridge University Press, Cambridge, 2008).

[24] D. W. Hogg and D. Foreman-Mackey, Data analysis recipes: Using Markov Chain Monte Carlo, Astrophs. J. Suppl. Ser. **236**, 11 (2018).

[25] D. Foreman-Mackey, D. W. Hogg, D. Lang, and J. Goodman, emcee: The MCMC hammer, Publ. Astron. Soc. Pac. **125**, 306 (2013).